

Laser Materials and Technology Research Center of
General Physics Institute,
Russian Academy of Sciences

Final Report

**Solid-State Raman Converters
for High-Average Power Chemical Oxygen
Iodine Laser.**

(~~FILED~~ F61708 97W0212)

SPC 97- 4065

19980617 113

Moscow, 1998

DTIC QUALITY INSPECTED 1

DISTRIBUTION STATEMENT A
Approved for public release;
Distribution Unlimited

FINAL REPORT

"Solid State Raman Converter for High-Average Power Chemical Oxygen Iodine Laser"

Introduction.

Stimulated Raman Scattering (SRS) in solid state materials is a new extensively growing area in laser physics. SRS allows to change the laser radiation frequency with a certain frequency shift which is determined by spontaneous Raman spectra of nonlinear material. The first observation of stimulated Raman scattering in solids was published in 1963 [1]. The authors investigated SRS in diamond, calcite and α -sulfur single crystals. Since then the natural calcite crystal has become the most popular Raman material due to its comparatively large size and low cost. It has an intense quasi molecular SRS-active vibronic mode with the energy as large as 1086 cm^{-1} and linewidth about 1.2 cm^{-1} [2, 3]. The Raman gain coefficient was measured to be 5.5 cm/GW at 532 nm wavelength [4]. The diamond crystal has larger Raman frequency shift 1332 cm^{-1} and higher gain [5]. But due to its small dimensions and high cost it has not found practical applications as a Raman material.

In 1980 a number of new synthetic crystals, barium, sodium, and lead nitrates were proposed as perspective Raman laser materials [5]. These crystals have intense vibronic modes with the energy of about 1050 cm^{-1} , which correspond to the internal symmetrical vibrations of $[\text{NO}_3]$ molecular ion. The Raman gain in $\text{Ba}(\text{NO}_3)_2$ crystal was measured to be as high as 47 cm/GW at 532 nm wavelength [4]. The number of various laser configurations have shown that the quantum conversion efficiency of $\text{Ba}(\text{NO}_3)_2$ SRS shifter can be up to 80% for nanosecond laser pulses [7-9] even for IR radiation with much lower gain. This has lead to the availability of commercial solid state Raman lasers with special properties such as high efficiency and diffraction-limited beam quality at eye-safe wavelengths [10]. However, the SRS threshold for 25 ps pump pulses was found to be 10 times higher than that for nanosecond pulses due to long vibronic relaxation time [11]. This transient SRS was accompanied by wide angular scattering to higher Stokes and anti-Stokes components, that interferes in their application for picosecond pump pulses.

Ivanuk et al. [12] found that potassium gadolinium tungstate, $\text{KGd}(\text{WO}_4)_2$ exhibited efficient Raman properties. In spite of the fact that its Raman gain coefficient at 1064 nm (6 cm/GW) is twice less than that in barium nitrate (11 cm/GW), the KGW crystal found many practical applications for frequency shifting of picosecond laser radiation [12, 13]. Variations in the Raman scattering cross section and Raman mode linewidth are responsible for the difference in the

REPORT DOCUMENTATION PAGE			Form Approved OMB No. 0704-0188	
Public reporting burden for this collection of information is estimated to average 1 hour per response, including the time for reviewing instructions, searching existing data sources, gathering and maintaining the data needed, and completing and reviewing the collection of information. Send comments regarding this burden estimate or any other aspect of this collection of information, including suggestions for reducing this burden to Washington Headquarters Services, Directorate for Information Operations and Reports, 1215 Jefferson Davis Highway, Suite 1204, Arlington, VA 22202-4302, and to the Office of Management and Budget, Paperwork Reduction Project (0704-0188), Washington, DC 20503.				
1. AGENCY USE ONLY (Leave blank)		2. REPORT DATE 1998		3. REPORT TYPE AND DATES COVERED Final Report
4. TITLE AND SUBTITLE Solid-State Raman Converters for High-Average Power Chemical Oxygen Iodine Laser			5. FUNDING NUMBERS F6170897W0212	
6. AUTHOR(S) Prof Tasoltan Tazretovich Basiev				
7. PERFORMING ORGANIZATION NAME(S) AND ADDRESS(ES) Laser Materials and Technology Research Center of the General Physics Institute Vavilov St. 38 Moscow 117942 Russia			8. PERFORMING ORGANIZATION REPORT NUMBER N/A	
9. SPONSORING/MONITORING AGENCY NAME(S) AND ADDRESS(ES) EOARD PSC 802 BOX 14 FPO 09499-0200			10. SPONSORING/MONITORING AGENCY REPORT NUMBER SPC 97-4065	
11. SUPPLEMENTARY NOTES				
12a. DISTRIBUTION/AVAILABILITY STATEMENT Approved for public release; distribution is unlimited.			12b. DISTRIBUTION CODE A	
13. ABSTRACT (Maximum 200 words) This report results from a contract tasking Laser Materials and Technology Research Center of the General Physics Institute as follows: The contractor will investigate materials for high average power Raman conversion of 1.3 micron laser radiation.				
14. SUBJECT TERMS Non-linear Optics, Non-linear Optical Materials , Lasers			15. NUMBER OF PAGES 39	
			16. PRICE CODE N/A	
17. SECURITY CLASSIFICATION OF REPORT UNCLASSIFIED	18. SECURITY CLASSIFICATION OF THIS PAGE UNCLASSIFIED	19. SECURITY CLASSIFICATION OF ABSTRACT UNCLASSIFIED	20. LIMITATION OF ABSTRACT UL	

behaviour of the above SRS materials. The comparative investigation of SRS-active vibronic modes in some solids using spontaneous Raman spectroscopy are discussed below. The results are important to understand the Raman properties of crystals and to search new nonlinear materials with certain frequency shift and high SRS efficiency.

Theoretical approach.

For plane pump and Stokes waves, SRS is described as a coupling of the optical waves to the coherent material excitation [14]. In the moving frame (z, t) where the optical pulses are at rest, the set of coupled differential equations can be written as [15]:

$$\frac{\partial E_p(z, t)}{\partial z} = -K_p E_s A_Q \quad (1a)$$

$$\frac{\partial E_s(z, t)}{\partial z} = K_s E_p A_Q^* \quad (1b)$$

$$\left(\frac{\partial}{\partial t} + \Delta\Omega_R \right) A_Q^* = E_p^* E_s \quad (1c)$$

K_p and K_s are coupling coefficients which include the Raman susceptibility; E_p and E_s are the pump and Stokes optical field amplitudes, and A_Q is the amplitude of material excitation. $\Delta\Omega_R$ is the Raman linewidth which is for homogeneously broadened line equals $\Delta\Omega_R = (\pi T_R)^{-1}$, here T_R is the dephasing time. The theoretical treatment of the set of equations (1) can be found in [14-17]. Depending on the pump pulse duration two temporal cases: a steady-state and a transient can be considered. The steady state case is observed when the duration of the pump laser pulse is longer than the vibronic relaxation time ($\tau_p \gg T_R$),

In this case if there is no pump depletion, the solution for the Stokes amplitude is exponential with a plane wave gain coefficient given as $G_{ss} = K_s (\Delta\Omega_R)^{-1} |E_p|^2$. This solution is readily obtained from the coupled set (1) when it is noted that, no changes of A_Q occur for a constant pump: $dA_Q/dt = 0$. The criteria $\tau_p \gg T_R$ is rather strong and it can be relaxed to [15, 17]: $\tau_p > 2\pi G_{ss} l (\Delta\Omega_R)^{-1}$, for which the steady state solution is still well approximated.

The intensity of the first Stokes component can also be written as [18]:

$$I_{\text{stokes}}(l) = I_{\text{stokes}}(0) \exp\{g_{ss} I_{\text{pump}} l\} \quad (2)$$

Here $I_{\text{stokes}}(0)$ and $I_{\text{stokes}}(l)$ are Stokes intensities at the input and output of the Raman medium, I_{pump} is the pump intensity and l is the length of the nonlinear crystal. The g_{ss} is a steady state Raman gain coefficient which is determined by the Raman properties of nonlinear medium [18]:

$$g_{ss} = \frac{\lambda_p \lambda_s^2 N}{\hbar c \pi m_s^2 \Delta\Omega_R} \left(\frac{d\sigma}{d\Omega} \right) \quad (3)$$

Here N is the number of scattering centers, $\lambda_{p,s}$ are the pump and Stokes wavelengths, n_s - refractive index at λ_s and $d\sigma/d\Omega$ is the Raman scattering cross section. Thus, we can note that in the steady state case the Raman gain coefficient g_{ss} is linearly proportional to the Raman scattering cross section and inversely proportional to the linewidth of Raman transition. The Raman linewidth is determined by a mechanism of vibronic phase relaxation due to the phonon-phonon coupling in the medium [9]. The value of $(d\sigma/d\Omega) \cdot (\Delta\Omega_R)^{-1}$ can be measured as a maximum in the spontaneous Raman scattering spectrum and for simplicity we will denote it as Σ_{peak} .

After Wang [16] in the transient case ($\tau_p \gg T_R$) with no pump depletion Raman gain G_r equals:

$$G_r I = \ln \frac{|E_s(I)|}{|E_s(0)|} \cong 2 \left(K_s I \int_{-\infty}^{\tau_p} |E_p(t')|^2 dt' \right)^{1/2} \quad (4)$$

And for rectangular pump pulse with duration τ_p it can be rewritten as

$$G_r \approx \left(2K_s I |E_p|^2 t_l \right)^{1/2} = 2(G_{ss} I \Delta\Omega t_l)^{1/2} \quad (5)$$

One can see that the transient Raman gain is reduced with shortening pump pulse as $(\tau_p)^{1/2}$ and proportional to multiplication of $G_{ss} \cdot \Delta\Omega$, hence, it depends on integral cross section. The analytical expression for the Stokes amplitude for large amplification gain was found in [16] as

$$I_{Stokes}(I) = I_{Stokes}(0) \exp \left[2 \sqrt{ \left(I_{pump} I \frac{8\pi^2 c^2 N}{\hbar \omega_{Stokes}^3 n^2} \left(\frac{d\sigma}{d\Omega} \right) \right) - \pi c \Delta\Omega_R \tau_p } \right] \quad (6)$$

From (6) one can see that for large amplification when the second term in the exponent gain is small the Raman gain is proportional to the square root of the total integral Raman scattering cross section $d\sigma/d\Omega$. It can be measured as an integral value of the Raman line intensity in spontaneous Raman scattering spectrum and we denoted it as $\Sigma_{int} = d\sigma/d\Omega$.

Below we will compare spectroscopic characteristics Σ_{peak} and Σ_{int} in different materials in order to characterize their SRS features for the Raman laser development.

Raman spectra comparative study for insulating crystals

The experiments on spontaneous Raman spectroscopy utilized the excitation by a CW argon ion laser, working at 488 nm wavelength. Block-scheme of Raman spectrometer is presented on Fig.1. The laser intensity at the sample was about 1 W. Raman spectrum was recorded by double-spectrometer "Spex-1403" in backwards scattering scheme. The spectral resolution of the system was 0.2-1.0 cm^{-1} . The argon laser plasma discharge lines were cut by an additional

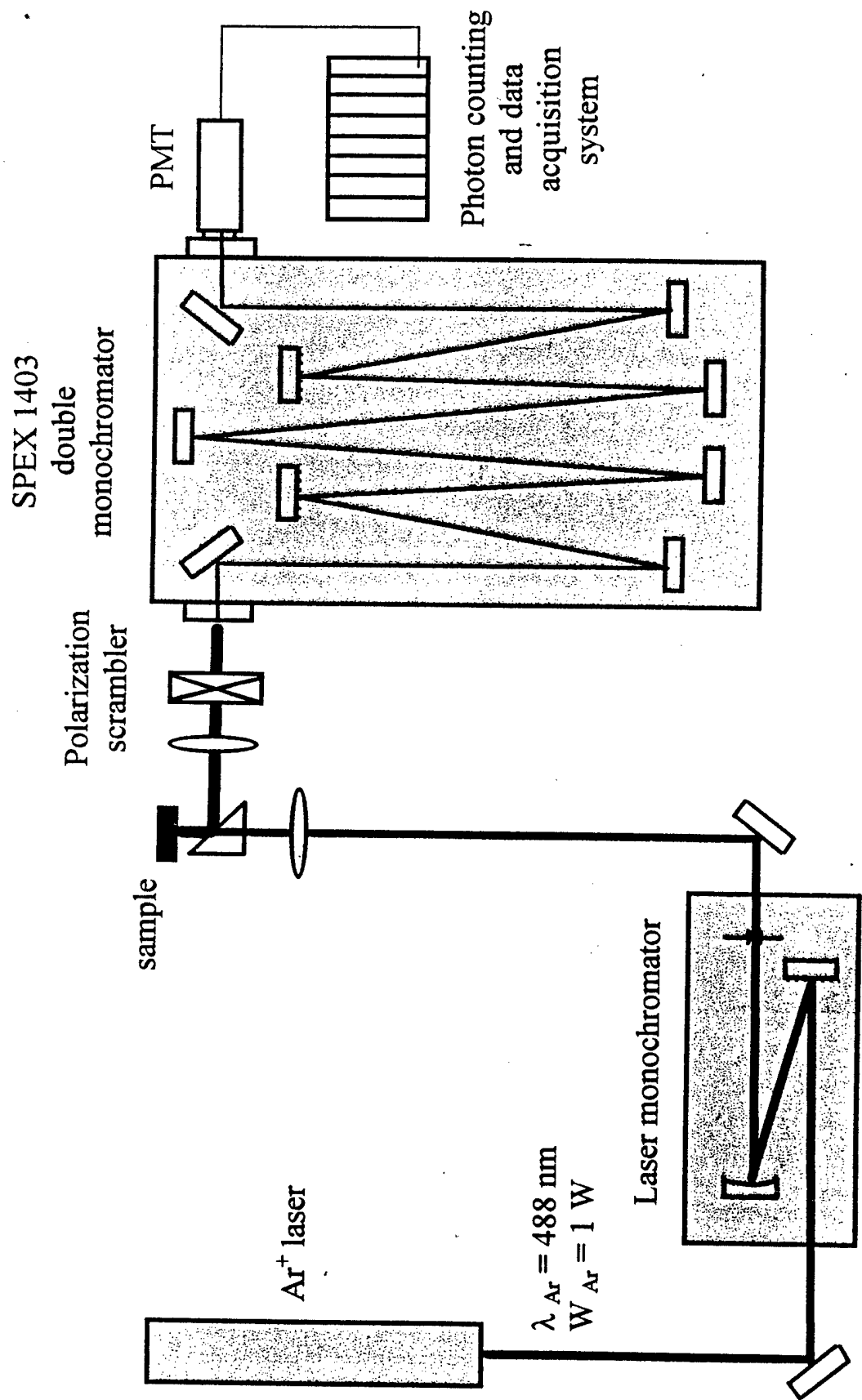


Fig. 1

EXPERIMENTAL SETUP FOR SPONTANEOUS RAMAN SPECTROSCOPY

premonochromator. To compensate the self polarization of spectrometer, a polarization scrambler was placed in front of the entrance slit.

Single crystal as well as polycrystal samples were investigated in our experiments. To compare integral and peak scattering cross sections in different crystals the plane-parallel samples were made from single crystals with the thickness either 0.7 or 2 mm. The diamond single crystal 0.7 mm thick with slope facets was used as a control sample.

The exciting laser intensity and spectrometer slit width had constant values in different sets of measurements. Focusing of exciting radiation and collimation of scattered light were the same in all the experiments. Since the Raman scattering was excited by a polarized beam, for some samples we made several experiments with different orientation of the sample crystallographic axes with respect to the direction of electrical vector E of the exciting beam. The conditions of the Raman scattering excitation of our measurements were very close to those of Raman lasers with longitudinal pumping.

The registered Raman spectra was analyzed with software fitting program which allowed to obtain values for Raman linewidth, peak and integral cross sections. The accuracy of the Raman linewidth was determined by the spectral resolution of the system and the widths of the slits. Except narrow lines ($\Delta\nu < 1 \text{ cm}^{-1}$), the spectral resolution was about 10% of the measured linewidth value.

The peak cross section value Σ_{peak} was measured with the accuracy of 10% for broad lines, while for narrow lines it became higher (~20%) due to spectral resolution limitation. While the accuracy for Σ_{int} was about 10% for narrow lines and increased to 20-40% due to uncertainty of the spectrum background level.

The measured Raman spectra are presented on Figs. 2-6.

The data we got from these spectra treatment are presented in Table 1.

Table 1. Spontaneous Raman scattering parameters of crystals

Material	Lattice space group	Molecular group	Raman freq. Ω_R (cm^{-1})	Raman line width $\Delta\Omega$ (cm^{-1})	Integral cross section Σ_{int} (a.u.)	Peak intensity Σ_{peak} (a.u.)	Scattering geometry of excitation	
							K	E
Diamond	O_h^7	-	1332.9	2.7	100	100	//C ₃	\perp C ₃
NITRATES AND CALCITE								
Ba(NO ₃) ₂	T_h^6	[NO ₃]	1048.6	0.4	21	63	//C ₄	//C ₄
NaNO ₃	D_{3d}^6	---	1069.2	1.0	23	44	//C ₃	\perp C ₃
CaCO ₃	D_{3d}^6	[CO ₃]	1086.4	1.2	6.0	10.6	//C ₃	\perp C ₃

TUNGSTATES

CaWO ₄	C _{4h} ⁶	[WO ₄]	910.7	4.8	47	18.6	⊥ C ₄	//C ₄
SrWO ₄ *	“-	“-	921.5	3	-	-	-	-
BaWO ₄ *	“-	“-	926.5	2.2	-	-	-	-
NaGd(WO ₄) ₂ *	“-	“-	919	14*	-	-	-	-
NaY(WO ₄) ₂ *	“-	“-	918	15*	-	-	-	-
Sc ₂ (WO ₄) ₃ *	-	“-	1024	15	-	-	-	-
In ₂ (WO ₄) ₃ *	-	“-	1023	13	-	-	-	-
LiIn(WO ₄) ₂ *	-	“-	920	8	-	-	-	-
NaSr(WO ₄) ₂ *			924	2.5				
Na ₂ WO ₄ *	O _h ⁷		929.2	1.8				
KGd(WO ₄) ₂	C _{2h} ⁶	[WO ₆]	901	5.4	50	35	⊥ C ₂	⊥ C ₂
“-	“-	“-	901	5.4	43	30	⊥ C ₂	//C ₂
“-	“-	“-	768	6.4	19	9.2	⊥ C ₂	⊥ C ₂
“-	“-	“-	768	6.4	59	37	⊥ C ₂	//C ₂
KY(WO ₄) ₂	“-	“-	905.6	7	46	35	⊥ C ₂	⊥ C ₂
“-	“-	“-	905.6	7	41	30	⊥ C ₂	//C ₂
“-	“-	“-	767.4	8.4	17	10	⊥ C ₂	⊥ C ₂
“-	“-	“-	767.4	8.4	58	35	⊥ C ₂	//C ₂
KYb(WO ₄) ₂	“-	“-	908	7.4	48	34	⊥ C ₂	⊥ C ₂
“-	“-	“-	908	7.4	48	34	⊥ C ₂	//C ₂
“-	“-	“-	757	15**	18**	13.8**	⊥ C ₂	⊥ C ₂
“-	“-	“-	757	15**	58**	30**	⊥ C ₂	//C ₂

IODATE AND NIOBATES

LiIO ₃	C ₆ ⁶	[IO ₃]	821.6	5.0	54	25	//C ₂	⊥C ₂
LiNbO ₃	C _{3v} ⁶	[NbO ₆]	872	21.4	44	5	//C ₃	⊥C ₃
“-	“-	“-	632	27	166	18	⊥C ₃	//C ₃
“-	“-	“-	250	28	-	22	⊥C ₃	//C ₃
LaNbO ₄	C _{2h} ³	[NbO ₄]	805	9	22	7.1	⊥C ₂	//C ₂

PHOSPHATES

Ca ₅ (PO ₄) ₃ F	C _{6h} ²	[PO ₄]	964.7	2.8	3.4	3.8	⊥C ₆	//C ₆
Sr ₅ (PO ₄) ₃ F	“-	“-	950.3	2.8	3.4	3.8	⊥C ₆	//C ₆

LiPO ₄ *	-	-	951	7.7	-	-	-	-
OTHER								
NaClO ₃ ***	-	[ClO ₃]	937	4.9**	-	-	-	-
NaBrO ₃ ***	-	[BrO ₃]	799.5	2.5**	-	-	-	-
NH ₄ Cl***	O _h ¹	[NH ₄]	1712	6	-	-	-	-
-	-	-	3052	85**	-	-	-	-
NH ₄ SO ₄ ***	-	[SO ₄]	976.5	3.5	-	-	-	-
Ba ₃ (B ₃ O ₆) ₂	C _{3v} ⁶	[B ₃ O ₆]	636	4.5	1	0.6	//C ₃	⊥C ₃
SiO ₂	D ₃ ⁶	[SiO ₄]	464	7	2.2	1.2	⊥C ₃	//C ₃

* - polycrystal sample

** - line with inhomogenous splitting

*** - crystal without orientation

Since the diamond sample exhibited one of the most intensive Raman lines, the values of Σ_{int} and Σ_{peak} for other investigated materials were normalized to those of the diamond. As we have seen above the integral Raman scattering cross section Σ_{int} determines the Raman gain coefficient in the transient case. Comparison of the Σ_{int} in different materials shows that high values are observed in lithium niobate for 632 cm⁻¹ mode (166%), diamond (100%), lithium iodate (54%) and some tungstate and molibdate (~50 ÷ 60%) crystals. Smaller values are observed in sodium and barium nitrate crystals (23% and 21%), calcite (6.0%), calcium and strontium appetites (3.4%), silica (2.2%) and BBO (1%) crystals. Our data explain why nowadays the KGW crystal is one of the most popular crystals for picosecond Raman operation with the large Stokes shift of 970 cm⁻¹ and the high moisture resistance. This material of large sizes, good optical quality, and moderate price is available in the market.

All tungstates crystals investigated can be divided into two groups: crystals with scheelite structure of C_{4h}⁶ space symmetry, and tungstates with monoclinic C_{2h}⁶ structure. For the first group the most intensive Raman line belongs to the symmetrical valent vibration of [WO₄] tetrahedron group, and in the second case, two intensive lines correspond to the vibrations of the bonds W-O in the linked [WO₆] octahedron [20].

Since the steady state Raman gain coefficient is defined by the value of peak scattering cross section Σ_{peak} which is determined by Raman mode linewidth, barium nitrate crystal is widely used as a Raman active material for practical applications. Integral cross section of SRS-active vibronic mode for nitrate Raman crystals is approximately 2 ÷ 3 times less than for tungstate ones. At the

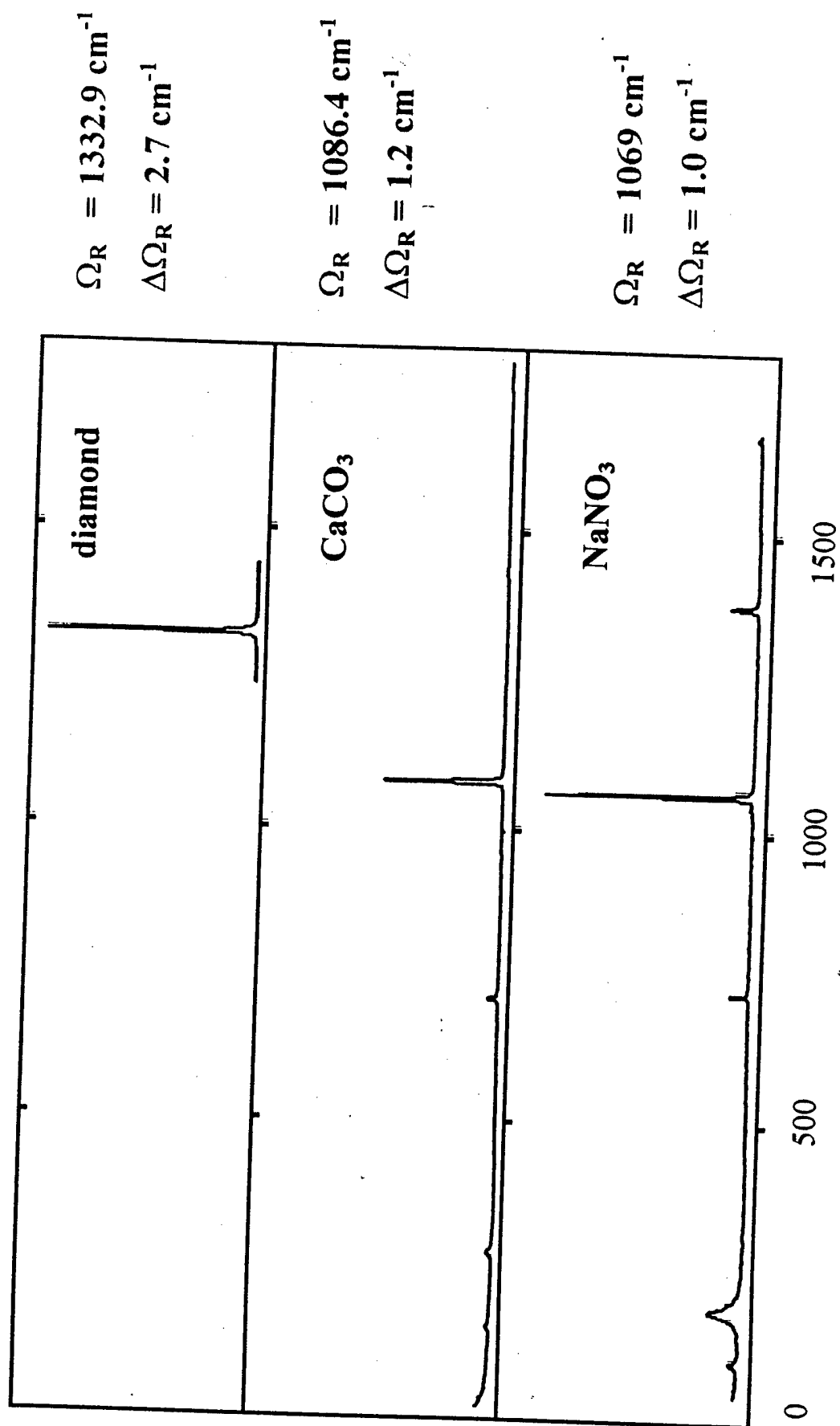


Fig. 2

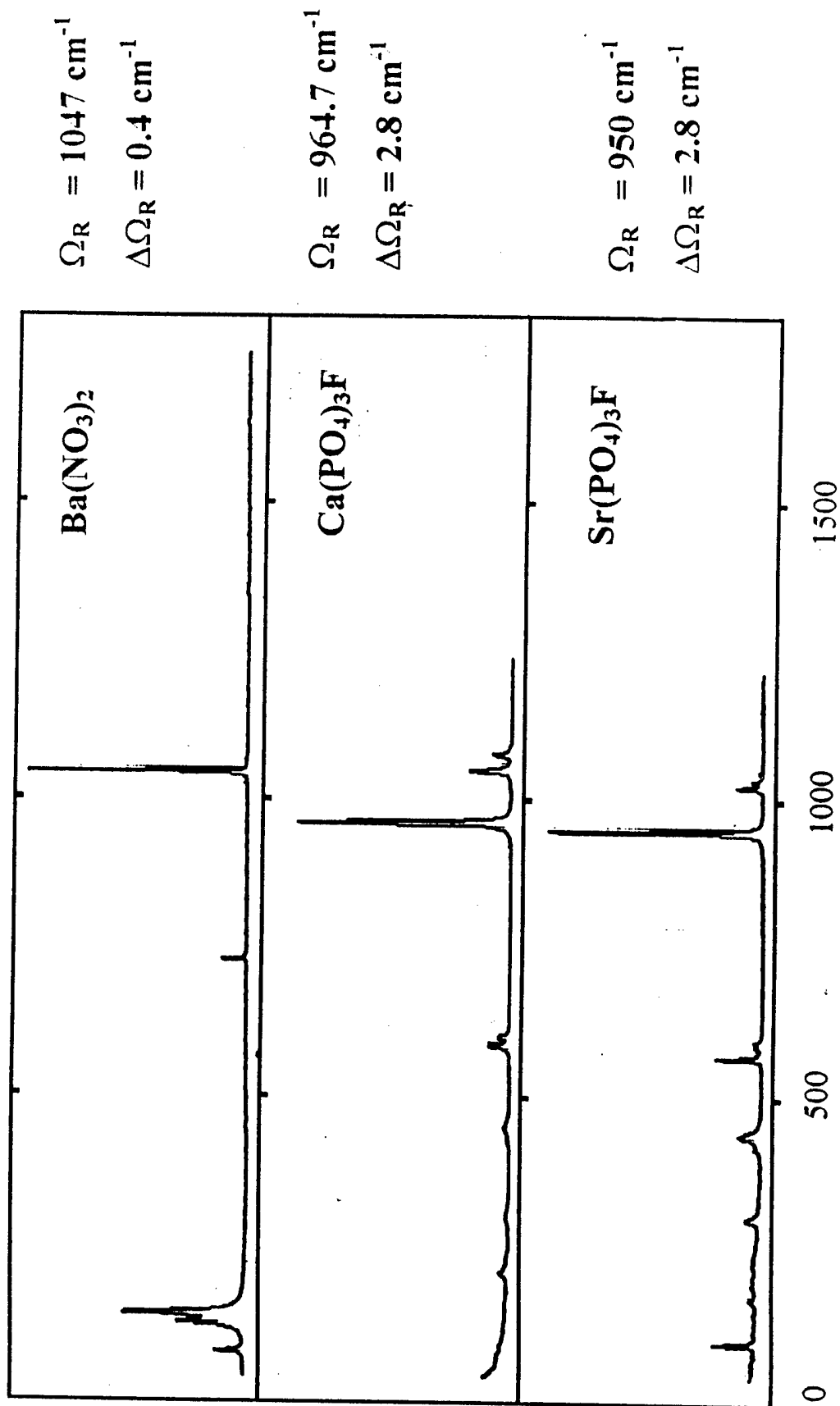
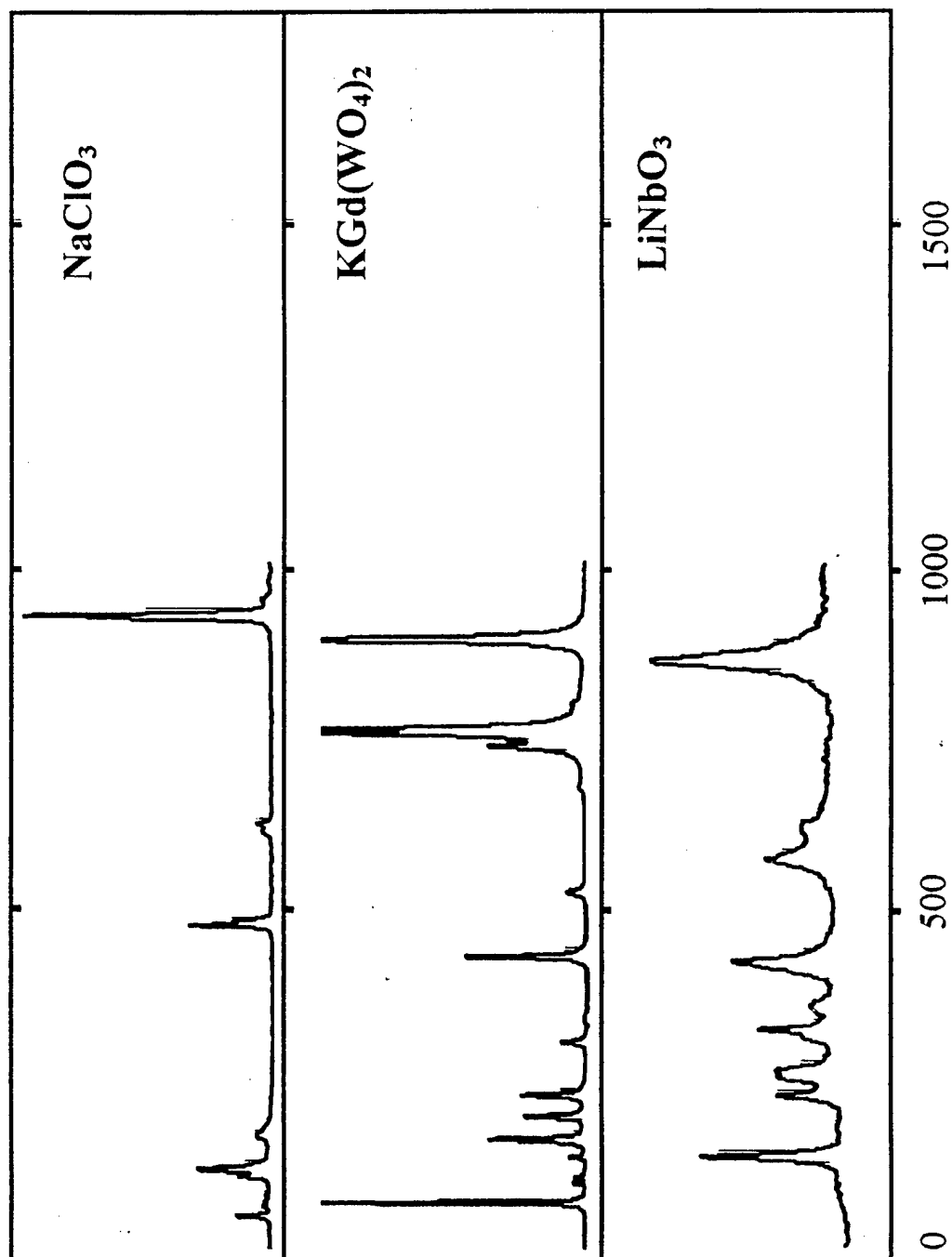


Fig. 3



$$\Omega_R = 937 \text{ cm}^{-1}$$

$$\Delta\Omega_R = 4.9 \text{ cm}^{-1}$$

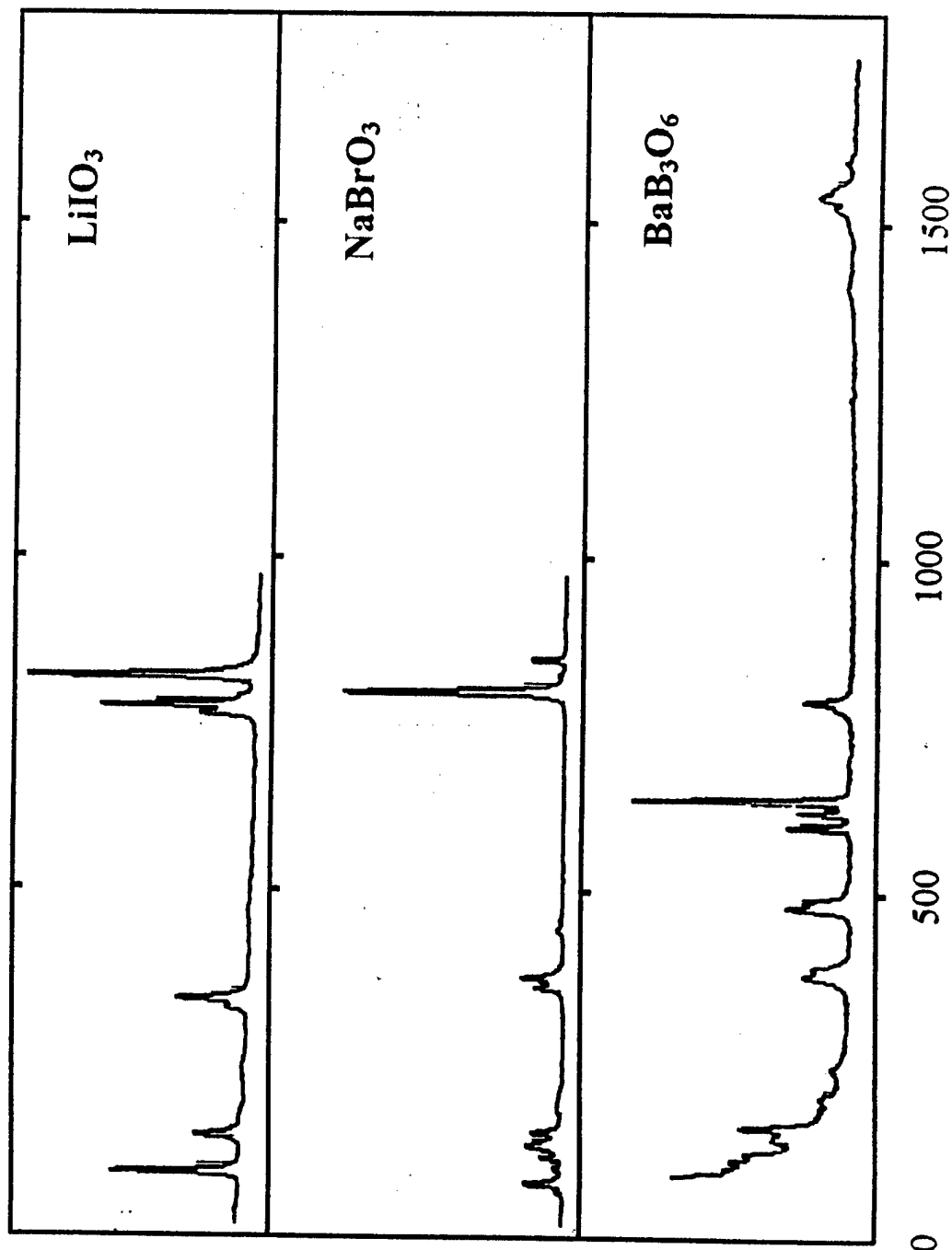
$$\Omega_R = 901 \text{ cm}^{-1}$$

$$\Delta\Omega_R = 5.4 \text{ cm}^{-1}$$

$$\Omega_R = 872 \text{ cm}^{-1}$$

$$\Delta\Omega_R = 21.4 \text{ cm}^{-1}$$

Fig. 4



$$\Omega_R = 821.6 \text{ cm}^{-1}$$

$$\Delta\Omega_R = 5.0 \text{ cm}^{-1}$$

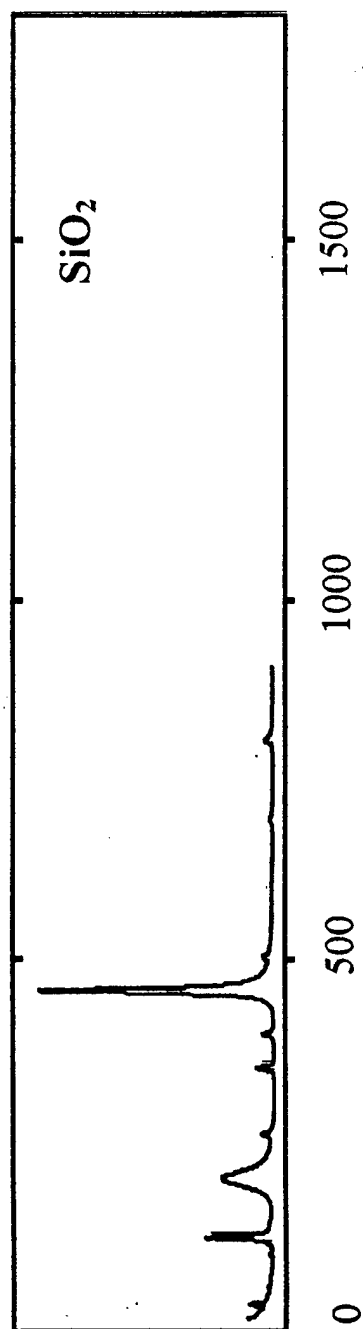
$$\Omega_R = 799.5 \text{ cm}^{-1}$$

$$\Delta\Omega_R = 2.5 \text{ cm}^{-1}$$

$$\Omega_R = 636 \text{ cm}^{-1}$$

$$\Delta\Omega_R = 4.5 \text{ cm}^{-1}$$

Fig. 5



$$\Omega_R = 464.5 \text{ cm}^{-1}$$

$$\Delta\Omega_R = 7.0 \text{ cm}^{-1}$$

Fig.6

same time, now the narrowest SRS-active lines in solids at room temperature were found in $\text{Ba}(\text{NO}_3)_2$ and NaNO_3 crystals. Their values were measured to be as small as $\Delta\Omega_{\text{Ba}(\text{NO}_3)_2} \approx 0.4 \text{ cm}^{-1}$ and $\Delta\Omega_{\text{NaNO}_3} \approx 1 \text{ cm}^{-1}$ which are correspondingly 7 and about 2 times less than that in the diamond. Authors [19] assigned the narrow linewidth in this Raman mode of $\text{Ba}(\text{NO}_3)_2$ crystal to the absence of the three phonon splitting relaxation process for this Raman mode. Due to this, the peak cross section Σ_{peak} of the Raman mode in $\text{Ba}(\text{NO}_3)_2$, measured in our experiments, exhibits the high value (60% of that in the diamond), that is twice higher than in KGW crystals. Due to wider linewidth NaNO_3 crystal has lower value of Σ_{peak} of only 44 %.

The linewidth of SRS-active mode in strontium and barium tungstates is 3 and 2.1 cm^{-1} , respectively. That is much less than in CaWO_4 and predicts the high peak cross section of about 30 and 40%. Lithium iodate and some tungstates have moderate spectral broadening $5 \div 8 \text{ cm}^{-1}$ and quite high values of peak cross sections from 37% to 10% depending on the crystal orientation. Raman mode (632 cm^{-1}) in lithium niobate crystal is much broader (27 cm^{-1}) but exhibits quite high value of Σ_{peak} (18%) due to the largest integral cross section (166%). Natural calcite demonstrates a comparable value of Σ_{peak} that is 10.6%.

Higher frequency Raman lines in lanthanum and lithium niobates (805 and 872 cm^{-1}) exhibit weaker Σ_{peak} of 7% and 5%, correspondingly. Calcium and strontium apatites have higher vibronic frequency bands and smaller values of peak Raman cross section ($\Sigma_{\text{peak}} = 3.8\%$). All these values are small but close to that of CaCO_3 crystal, which was successfully used for stimulated Raman scattering even for nanosecond pump pulses. Due to large frequency shift ($\Omega_R = 800 \div 960 \text{ cm}^{-1}$) and broad linewidth ($\Delta\Omega = 3 \div 20 \text{ cm}^{-1}$), the above-mentioned niobate and apatite crystals can be useful for SRS of picosecond laser pulses.

Some other Raman materials presented in Table 1 can attract interest due to different values of Raman frequency, but they have rather small values of integral and peak cross sections, which lead to much higher SRS thresholds.

Thermoconductivity of crystalline materials

Advantages and drawbacks of solid state Raman materials for high power laser frequency Raman shifters and Raman lasers were analyzed.

The main advantage of solid state Raman devices is their compactness due to much higher concentration of Raman active oscillators in crystals ($N=10^{22} - 10^{23} \text{ cm}^{-3}$) than even in high pressure gases ($N=2.5 \cdot 10^{20} \text{ cm}^{-3}$ for hydrogen at $P=10 \text{ atm}$ at $T=300 \text{ K}$). As a result, about 100 times shorter length of light to matter interaction can be used. At the same time, the decrease of

Raman cell length from ~ 1 meter in case of H_2 or N_2 molecular gases to a few centimeters for crystals leads to the problems of heat removal from the small volume. So, one of the main characteristics for powerful Raman lasers is thermoconductivity of Raman crystals.

We carried out analysis of literature data on thermoconductivity of great number of crystals, both insulator and semiconductor. The potential candidates for Raman shifters and lasers from the view-point of high thermoconductivity are presented in Table 2.

Table 2.

Thermoconductivity of some insulators and semiconductors, perspective for high average power Raman lasers and shifters (W/m.K).

Insulators			Semiconductors		
Crystal	300K	77K	Crystal	300K	77K
Diamond	550		SiC	490	4100
BeO	370	6700	AlN	200	290
MgO	58	460	BN	180	43
Al ₂ O ₃	35	1100	Si	156	1500
Y ₂ O ₃	27		GaP	140	450
SiO ₂	14.3	60	AlSb	69	210
LiF	14		InP	70	470
YAG	13		GaAs	58	270
CaF ₂	12.5	60	ZnO	54	260
SrTiO ₃	12	18	GaSb	36	180
NaF	9.2	130	ZnS	27	155
BaTiO ₃	5		CdS	20	97
LiNbO ₃	4.6	12.6-16	ZnSe	19	
LiTaO ₃	4	1.6	InSb	19	
KGd(WO ₄) ₂	2.6-3.8				
PbMoO ₄	1.5				
KDP	0.7-1.7				
Ba(NO ₃) ₂	0.7-1.7				

As one can see, some of them show very high thermoconductivity at $T=300$ K and even much higher at $T=77$ K in comparison with well known Raman laser crystals, nitrates and tungstates.

Insulating crystals as candidates for high power Raman laser

Analyzing the above given data on thermoconductivity and cross-sections, we can compare insulating crystal properties from the view-point of their application as high power Raman laser media. We also have studied yttrium oxide (Y_2O_3) and sapphire (Al_2O_3) crystals. The comparative spectra of Raman scattering for the both materials are given on Fig. 7. We found that the integral Raman scattering cross-section of Y_2O_3 is 66 times higher, and the peak cross-section is 30 times higher than that of Al_2O_3 .

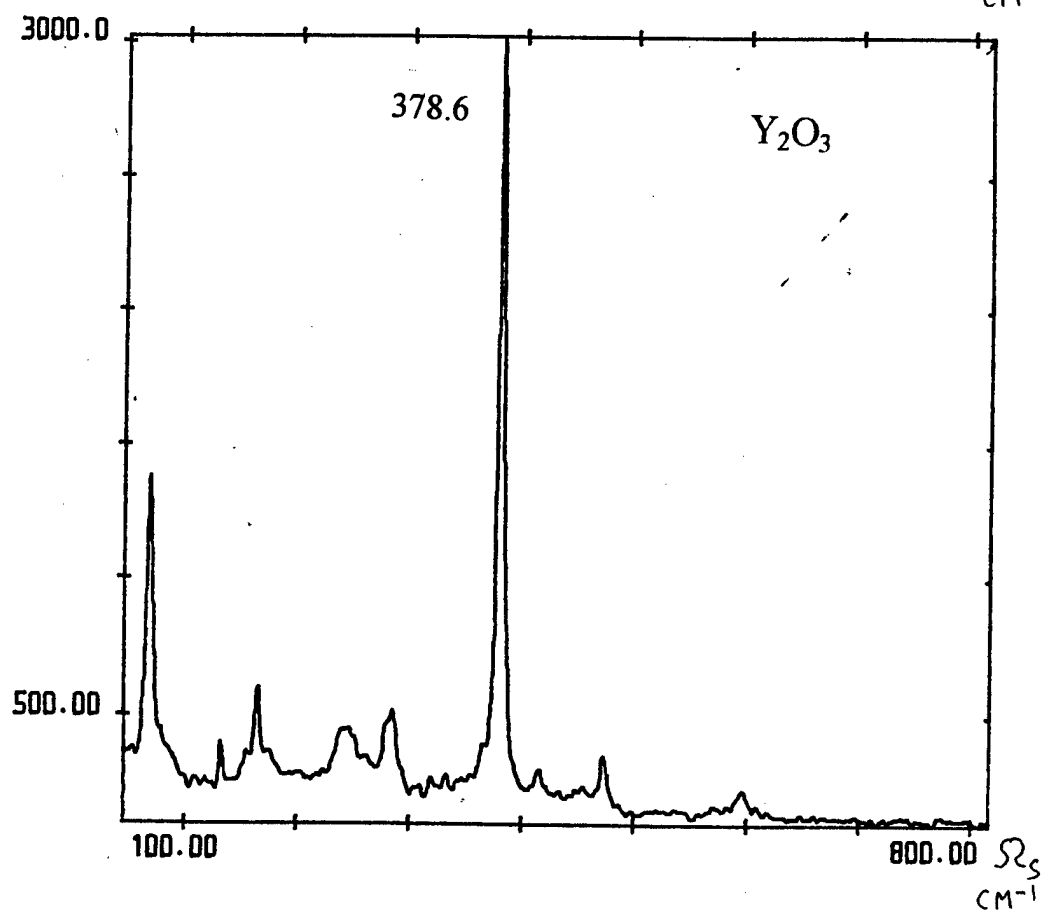
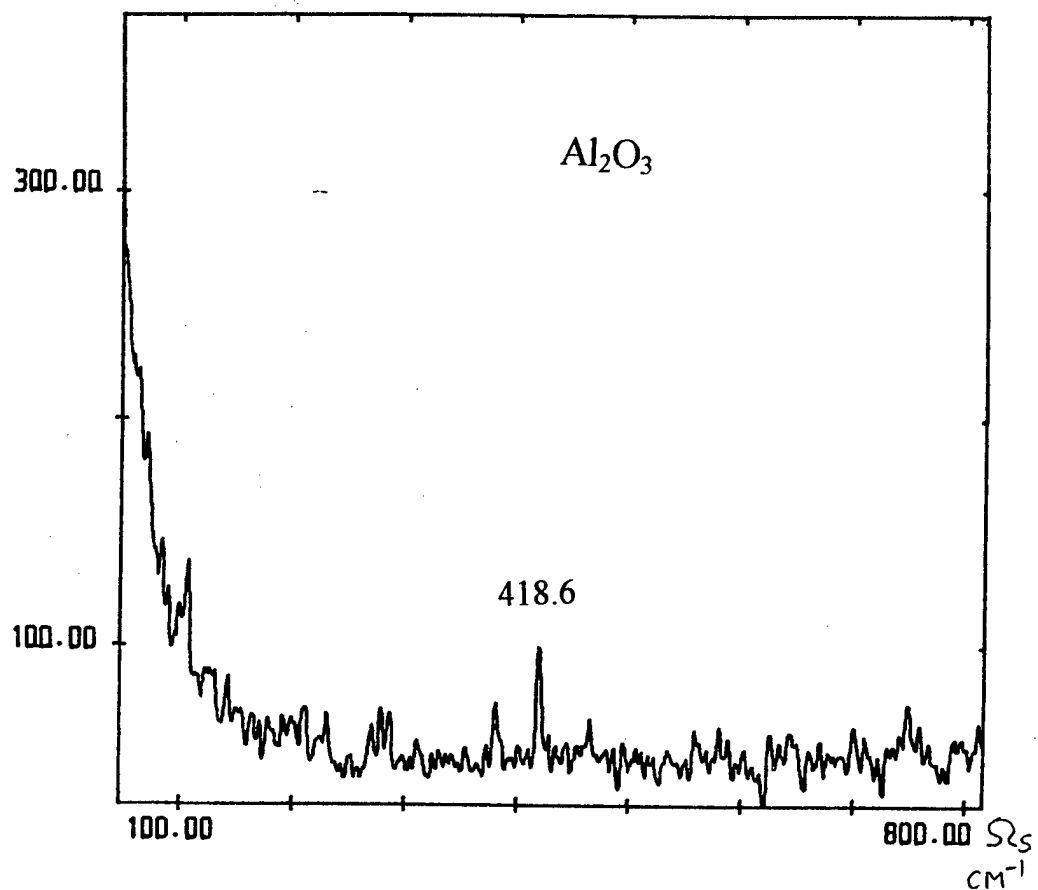
Comparison data for the studied crystals are presented in Table. 3.

Table 3.

Crystal	Ω cm^{-1}	$\Delta\Omega$ cm^{-1}	Σ_{int} (a.u.)	Σ_{peak} (a.u.)	Therm. cond. W/mK
Diamond	1332.9	2.7	100.0	100.0	550
KGW	901.0	5.4	50.0	22.0	2.6-3.8
	768.0	6.4	59.3	23.0	-"-
CaWO ₄	910.7	4.8	47	18.6	-
SrWO ₄	921.5	3	-	30*	-
BaWO ₄	926.5	2.2	-	40*	-
NaSr(WO ₄) ₂	924	2.5	-	-	-
NaWO ₄	929.2	1.8	-	-	-
LiNbO ₃	250	27	-	22	4.6 ¹
	632	27	166	18	-"-
	872.0	21.4	44	5.0	-"-
LaNbO ₄	807.0	9.0	22.0	7.1	-
Y ₂ O ₃	378.6	4.0	3.3	2.16	27
SiO ₂	464.5	7.0	2.2	1.2	14
Al ₂ O ₃	418.6	2.0	0.05	0.07	35

* Estimated

Fig. 7



Analyzing Table 3, one can see that among the dielectric crystals only diamond has a unique set of properties: the large Stokes shift, narrow spectral width, extraordinary high values of integral and peak cross-section, together with extremely high thermal conductivity coefficients. The main drawbacks of the diamond are not sufficient optical quality, low availability and high price of big crystals. The properties of the other crystals are not so uniform with respect to their application in powerful Raman devices. In particular, tungstate crystals $\text{KGd}(\text{WO}_4)_2$, CaWO_4 , SrWO_4 , and BaWO_4 have high integral and peak cross-sections but moderate thermal conductivity; LiNbO_3 crystals have a little higher thermal conductivity but lower peak cross-sections of Raman scattering; crystal Y_2O_3 has much better thermal conductivity than LiNbO_3 and tungstates, but its integral and peak cross-sections are much less than those of lithium niobate; quartz crystal is almost twice poorer than Y_2O_3 both in thermoconductivity and cross-sections, sapphire crystal with its high thermal conductivity shows the lowest values of Raman scattering cross-sections.

Raman spectroscopy of natural diamonds.

Diamond has O_h space group symmetry of crystal unit cell, which contains 2 carbon atoms. Only one lattice F_{2g} symmetry vibration is Raman active, with the polarizability tensors

0 0 0	0 0 d	0 d 0
0 0 d	0 0 0	d 0 0
0 d 0	d 0 0	0 0 0

The F_{2g} Raman line intensity in the diamond spectrum depends scattering geometry and crystal orientation. We used the back scattering geometry with parallel excitation and scattering light directions. The excitation light electrical vector E was perpendicular to the scattering plane. We did not use an analyzer for scattering light measurements.

Five samples were investigated. The first sample about 0.7 mm thick was faceted and had a polished $[111]$ plane as an entrance face. The second sample 0.2 mm thick had two polished $[110]$ planes. Three other samples were faceted to jewelry standard.

Taking into account the scattering geometry used in our experiments, one can estimate the diamond Raman line intensity as $\sim d^2$ for $[110]$ orientation and $\sim 5/3 d^2$ for $[111]$ one. This calculated intensity were experimentally confirmed in our measurements with accuracy of 20%. Thus, the $[111]$ plane of diamond crystal is preferable as an entrance face for Raman scattering.

The Raman spectra of these crystals are presented in Fig. 8 and 9.

Fig. 8

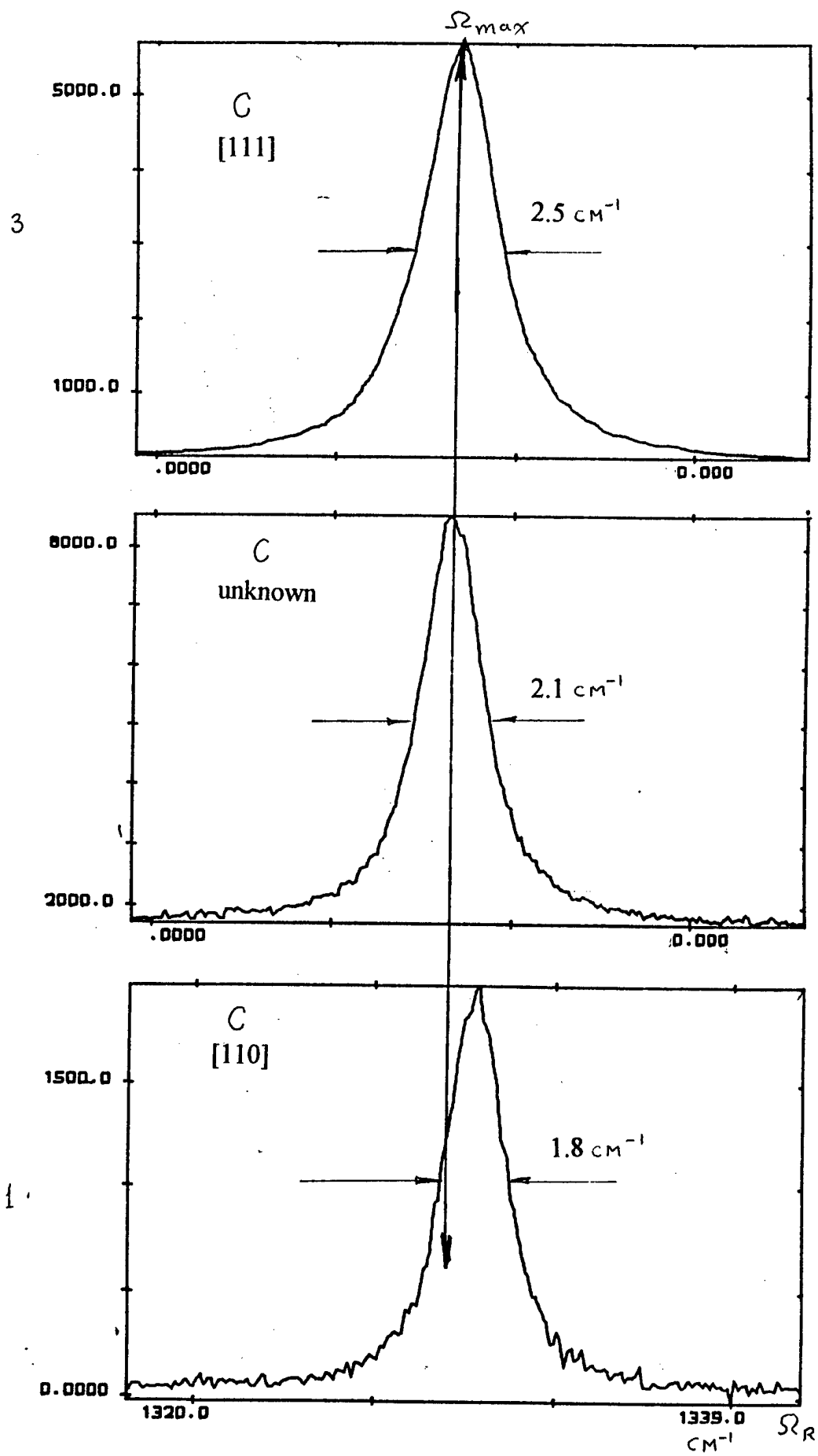
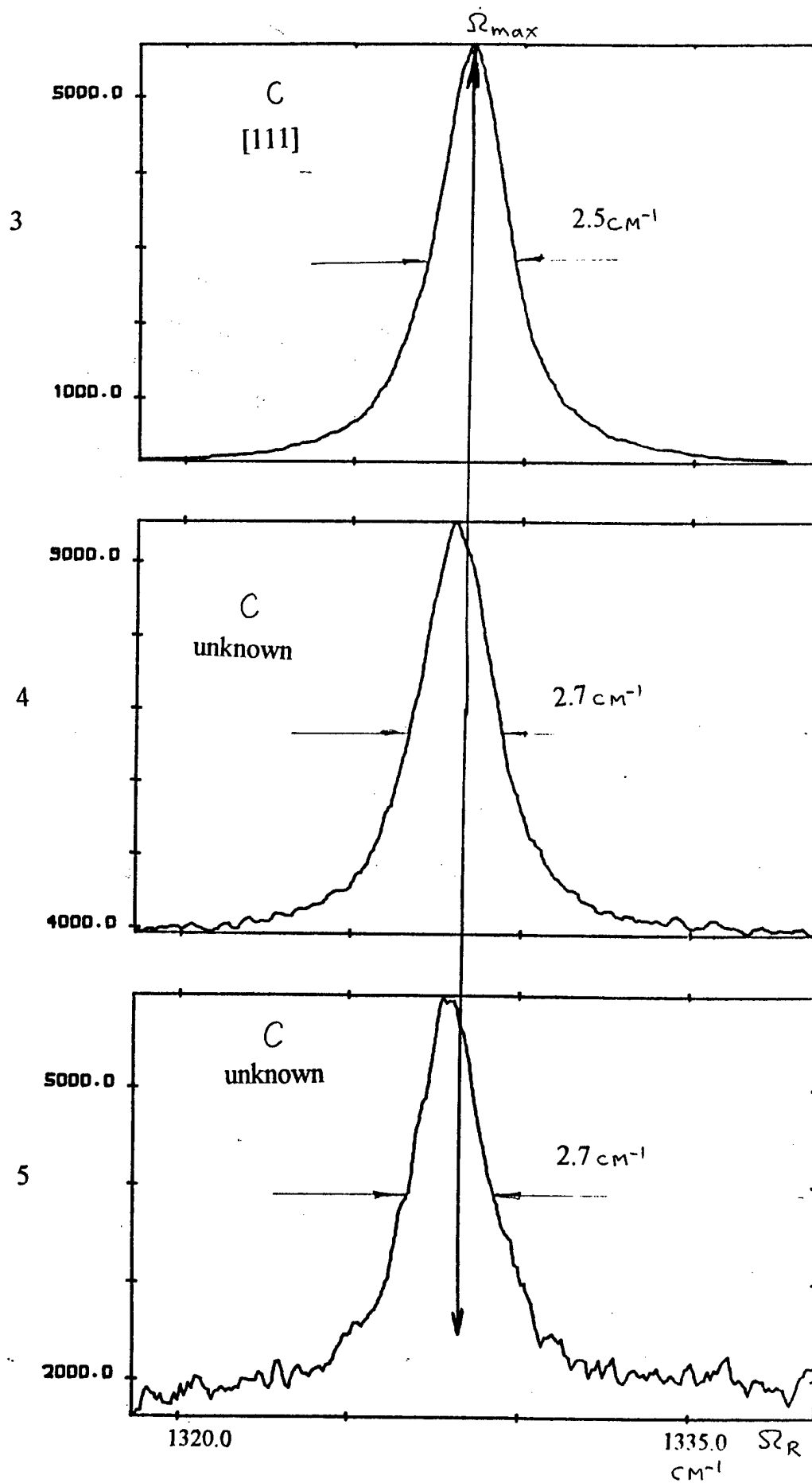


Fig. 9



The comparison of scattering spectrum peak positions and F_{2g} Raman line spectral linewidths on half maximum for the studied natural diamond samples is given in Table 4.

Table 4.

N	Orientation	Peak position Ω_{\max} (cm ⁻¹)	Measured linewidth, $\Delta\Omega_{\text{meas}}$ (cm ⁻¹)	Inhomogeneous linewidth, Δ_{in} (cm ⁻¹)
1	[110]	1333.4	1.8	0.5
2	unknown	1332.8	2.1	0.95
3	[111]	1332.9	2.5	1.4
4	unknown	1332.5	2.7	1.6
5	unknown	1332.5	2.7	1.6

As one can see, there are deviations of about 0.9 cm⁻¹ in the peak positions and linewidths. From the data of Table 3 we can find some correlation between the peak position and linewidth of the Raman line when moving from one crystal to another. Crystals with the smallest linewidth show the highest peak frequency, and crystals with the highest linewidths show smaller F_{2g} Raman line frequency.

It can be supposed that such deviations of linewidths in natural diamond have inhomogeneous character and are caused by statistically distributed impurities.

Analysis of Raman scattering line shapes show that this could be well fit with the help of Voigt profile resulting when a spectral line is broadened simultaneously by Lorentz effect (homogeneous, or natural line broadening) and Gaussian effect (inhomogeneous broadening due to statistical distribution).

Homogeneous linewidth can be determined from the decay time measurements in transient Raman scattering experiments, and is equal to $\delta_L=1.65$ cm⁻¹ at T=300 K [21].

We deconvoluted the Gaussian inhomogeneous part of line broadening $\Delta\Omega_{\text{in}}$ from the measured Voigt broadening Δ_{meas} with the help of D.W. Posener table [22], taking into account the Lorentz homogeneous broadening $\delta_L=1.65$ cm⁻¹. The inhomogeneous linewidths for all the five samples are presented in Table 4. As one can see, the inhomogeneous broadening varies significantly, by the factor more than 3, in this set of natural diamonds. This strong variation can be responsible for valuable variation (of some tens percents) in the peak intensity and Raman gain of diamond.

We measured some of our samples before and after γ -irradiation. It should be noted that γ -irradiation by ⁶⁰Co with the dose of 10⁷ rad. does not broaden essentially the Raman line. However, such irradiation decreases the measured line contrast due to spectral background growth caused by additional absorption and luminescence of γ -irradiated samples.

GaP and diamond comparative Raman spectroscopy

To get data on Raman frequency, broadening, and integral and peak cross-section of gallium phosphide crystals having absorption edge at the wavelength of 600 nm in comparison with referenced diamond crystal, we used a Rodamin dye CW laser pumped by a CW argon laser oscillating at 620 nm with a good transparency. The comparison was done on a diamond thin plate 0.2 mm thick with [110] orientation and on a GaP thin plate 0.8 mm thick with orientation [100] and [111]. As the unit cell of GaP has T_d^2 space group symmetry without an inversion point, the F_2 Raman vibration splits into two components: longitudinal C_L and transverse C_T modes (see Fig.10). The calculation of intensities of these modes shows that C_L is the most intensive for [100] orientation in our back scattering geometry (Fig. 10, a). The C_T line intensity is equal to zero in this case. For [111] orientation, the C_T appears, but the C_L line intensity is only 5/9 from that for [100] orientation (Fig.10, b). Experimental data on Raman line peak and integral intensities for C_L vibration of GaP and for F_{2g} vibration of diamond for both orientations are presented in Table 5. The difference in thickness of diamond and GaP plates was taken into account.

Table 5.

Crystal	Orientation	Peak intensity Σ_{peak} (a.u.)	Integral cross-section Σ_{int} (a.u.)	Linewidth $\Delta\Omega_{\text{meas}}$ (cm^{-1})
Diamond	[111]	100	100	2.5
Diamond	[110]	70	80	1.8
GaP; C_L	[100]	260	170	1.7
GaP; C_L	[111]	140	87	1.7

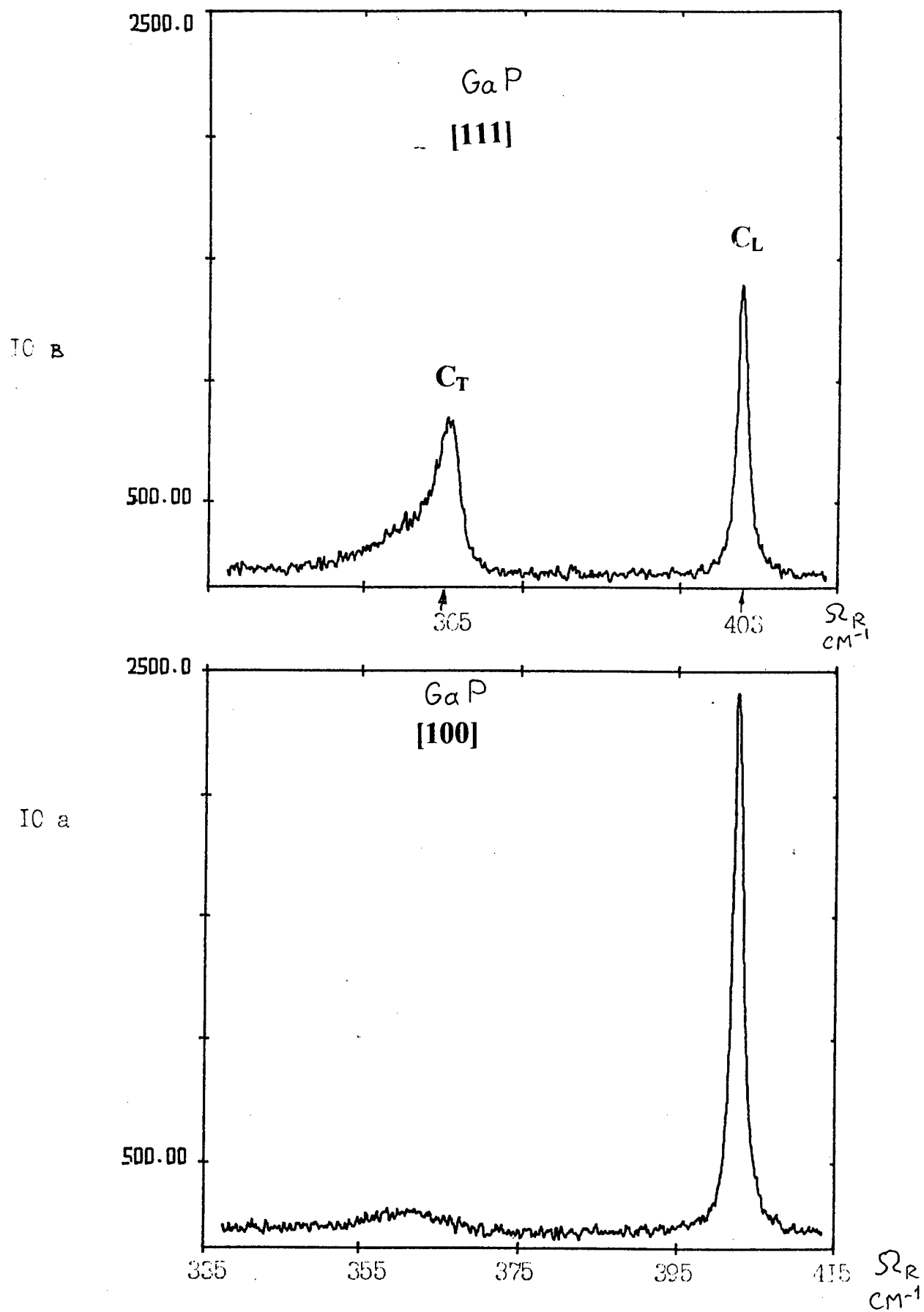
Like in Table 1 and Table 3, the cross-section data in Table 4 were normalized to [111] diamond data.

These data show that [100] orientation of GaP crystal is preferable when using this crystal as a Raman laser medium. To the contrary, as it was already shown above, the preferable laser orientation for diamond is [111].

Experimental setup optimization for comparative Raman spectroscopy in infrared.

During the reported period a number of infrared Raman spectrometers was assembled. One of them based on IR SDL-1 double monochromator with S-1 photomultiplier and a powerful

Fig. 10



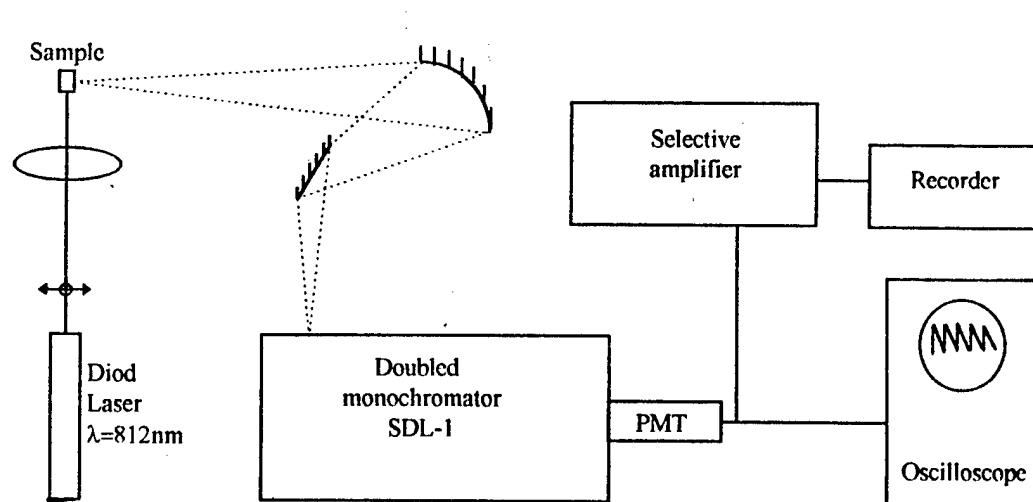
(0.5W) collimated CW diode laser ADLAS with temperature tuning and stabilization was assembled to measure IR Raman spectra with 812 nm wavelength pumping for narrow band gap material testing where argon and dye laser lines cannot be used due to strong band to band absorption. Block-scheme of this setup is shown in Fig.11. This installation successfully works and provides the possibility for Stokes Raman spectra measurements in IR spectral range. Fig.12 presents three Raman spectra of thick GaP crystals (of cubic form 6x6x5 mm), measured for different crystal surfaces in 90° rectangular scheme. Some intensity variations are observed in Lo ($\Delta\nu=404\text{ cm}^{-1}$) and To ($\Delta\nu=369\text{ cm}^{-1}$) phonon mode scattering. The main drawback of this setup is the very wide spectral width of the diode pump laser: $\Delta\nu=404\text{ cm}^{-1}$. This brings difficulty in separating closely lying Raman lines. At the same time, Raman and X-ray analysis of this large cubic GaP crystal shows a multiblock crystal structure with strong block to block angular misalignment.

For longer wavelengths of pumping $\lambda_p=1.047\mu\text{m}$ and $\lambda_p=1.064\mu\text{m}$, best results we got in an anti-Stokes Raman spectroscopy scheme where the pump beam wavelength λ_{pump} corresponds to minimum sensitivity of S-1 photocathode and Raman scattered light has higher frequency and shorter wavelength, which corresponds to higher S-1 photocathode sensitivity. Block-scheme of spectrometer is shown in Fig. 13. This spectrometer is based on DFS-12 high resolution double monochromator with S1 photocathode photomultiplier and the gated boxcar integrator PAR-162/164. Two Nd:YAG lasers ($\lambda=1.064\mu\text{m}$), one with low repetition rate of 12.5 - 50 pulses per second and high peak power of about 1 MW, and the second with high repetition rate of 10^4 pulses per second and medium peak power of about 1 kW, were used. To improve sensitivity of the Raman shifted light registration, the third, Nd:YLF laser working at $\lambda=1.047\mu\text{m}$ was used.

Examples of IR Raman scattering spectra under high peak power low repetition rate Nd:YAG nanosecond laser pumping are presented in Fig. 14 for two scattering geometries. Curve 1 corresponds to 90° rectangular scattering and curve 2 corresponds to 180° backscattering. The upper horizontal scale shows the real frequency of scattered light and the bottom horizontal scale is the difference between Raman and pump light frequencies: $\Omega_R=\Omega_p - \Omega_s$. As is seen, this spectrum demonstrates intensity variations for at least four most intensive Raman lines with Ω_R equal to 150, 220, 570, and 620 cm^{-1} .

By shortening the pump laser wavelength from 1.064 to 1.047 μm , we can improve the photomultiplier sensitivity for the whole Raman spectrum range and get better spectral resolution. An example of such a spectrum for 90° rectangular scattering geometry and quasi CW high repetition rate Nd:YLF nanosecond laser pumping is shown in Fig. 15. One can find 3 very strong narrow Raman lines at 150, 220, and 310 cm^{-1} . Smaller intensity of high frequency Raman

Fig. 11



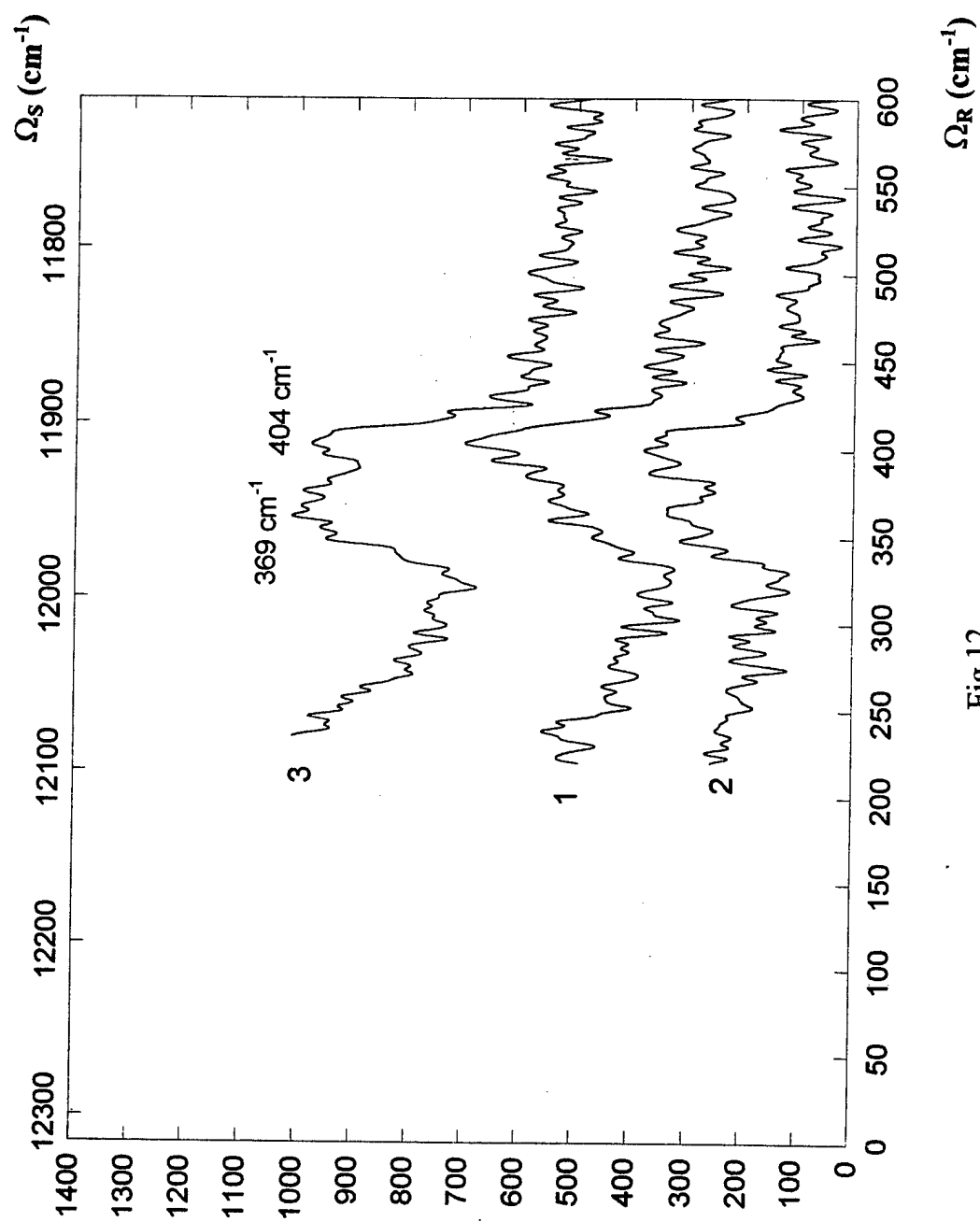


Fig.12

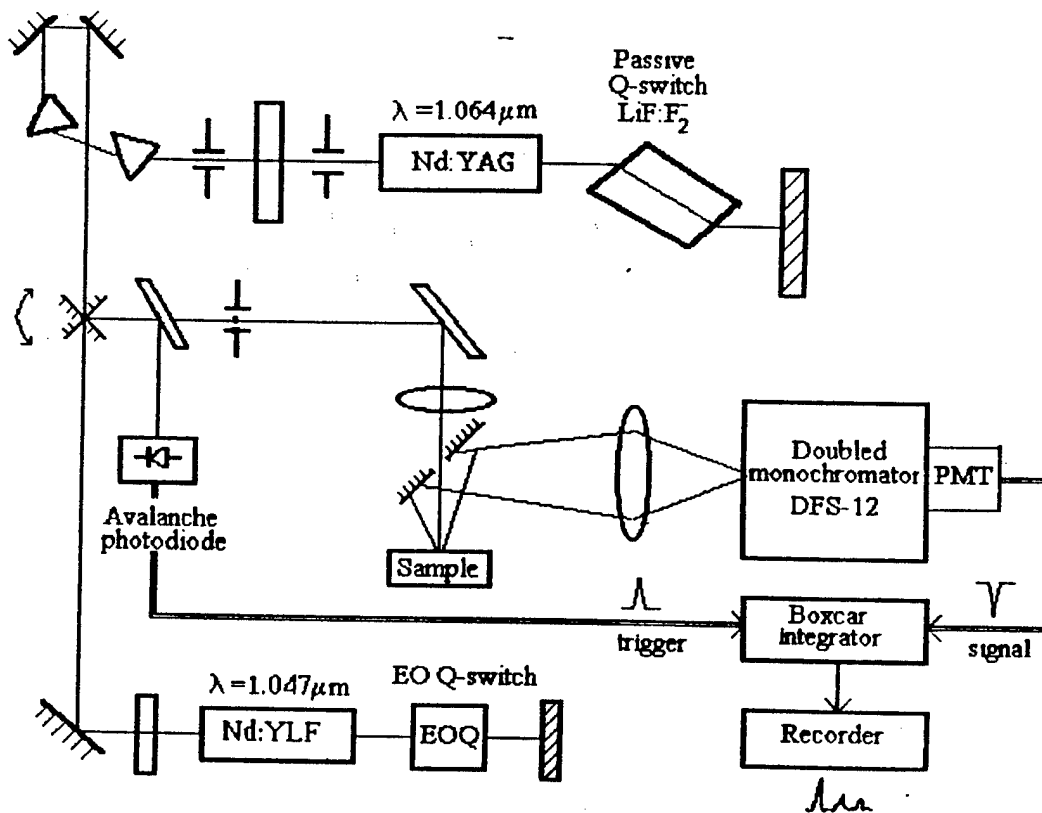


Fig. 13

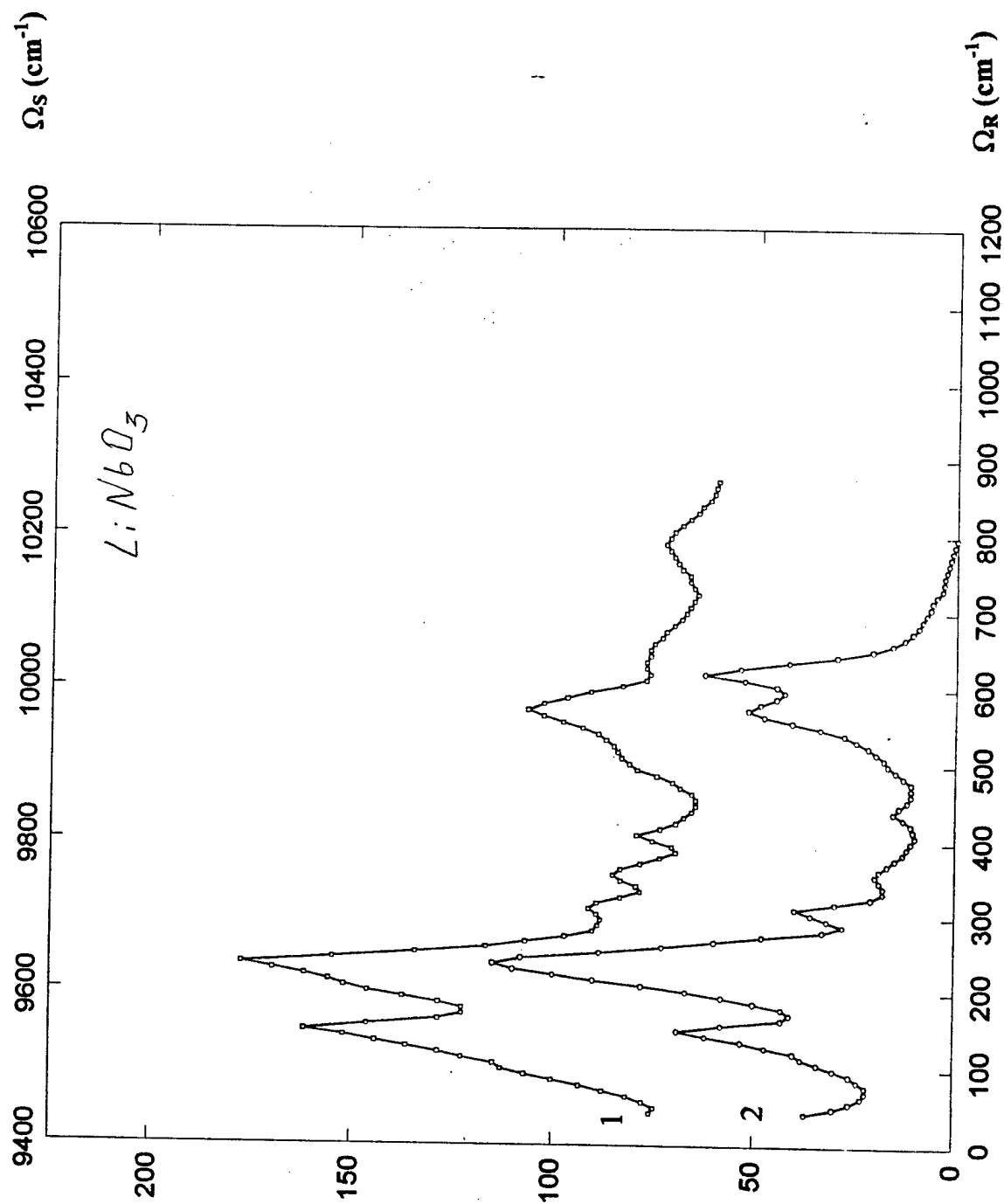


Fig. 14

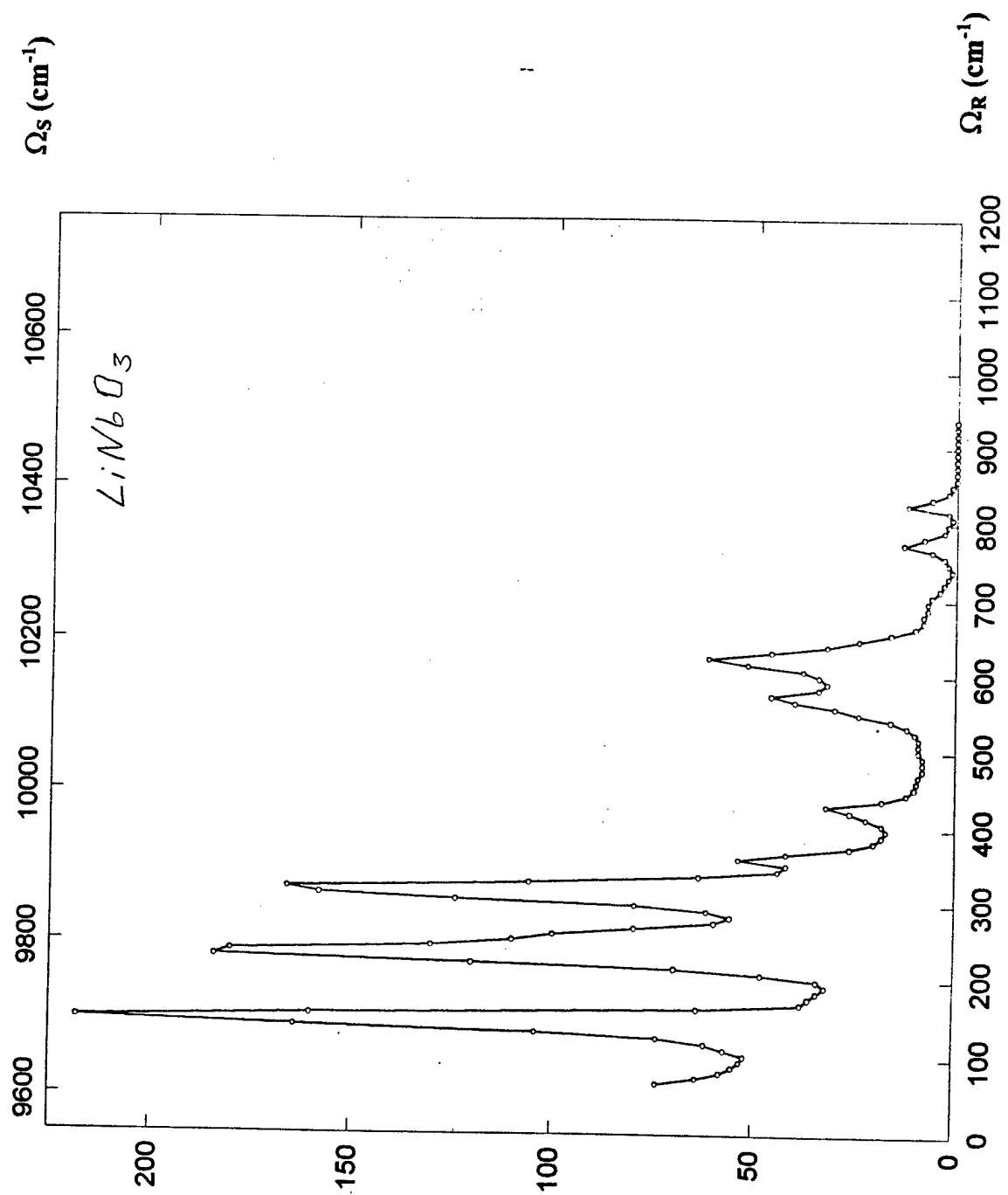


Fig.15

scattering at 570 and 620 cm^{-1} on this spectrum is due to much smaller phonon occupation number $n(\Omega_R; T) \sim e^{-\Omega_R/kT}$ for this anti-Stokes scheme at room temperature ($kT \sim 210 \text{ cm}^{-1}$).

Linear and nonlinear IR light absorption in GaP and Si semiconductor materials.

The absorption spectra of semiconductor materials were measured using the standard two channel photometer within 400-2500 nm range and registered by personal computer. To avoid the influence of Fresnel losses on the measured residual absorption the polished plate of the same material with absorption much less than that for tested sample was inserted into the second compensating channel. These spectra were then recalculated into the absorption coefficient spectra using the thickness of the sample as the difference between the thickness of two plates.

The curve 1 in Fig. 16 corresponds to the case of two GaP plates with thickness of 5 mm (Sample 1) and 0.4 mm (Sample 2) correspondingly in the sample and compensating channels. The analogous dependence for two Si samples with thickness 5 mm (Sample 3) and 0.5 mm (Sample 4) are presented by curve 2 in Fig. 16. It is clearly seen that short wavelength absorption edge for GaP is shifted far enough towards shorter wavelengths as compared to Si sample due to sufficiently high energy gap. The residual absorption in case of Fresnel losses compensation is observed to be at the level of 0.5 cm^{-1} for both cases. The presence of impurities in semiconductors leads to formation of shallow traps near the bottom of the forbidden zone shifting the absorption edge towards longer wavelengths. This can be demonstrated by curve 3 where the absorption curve for two plates 4.4 mm (Sample 5) and 0.75 mm (Sample 6) thick (placed correspondingly in sample and compensation channel) cut from one sample with rather small impurities concentration are shown. The short wavelength edge of absorption curve is seen to be shifted to the blue as compared to other GaP sample (Sample 1) measured in practically the same configuration.

The nonlinear absorption features were tested under the quasi cw excitation by Nd:YAG laser operating at 1.06 and 1.32 μm . The cavity of the 1.06 μm laser was formed by the concave total reflecting mirror with radius of 400 mm placed 150 mm apart the active element, flat output mirror with reflectivity about 87% and Br wster shape accousto-optic Q-switcher fabricated from crystalline quartz with high optical transmittance at both operating wavelengths. To maximize the output power of the laser in the zero order mode the polished active element 5 mm in diameter and 90 mm long was used. The laser emitted about 3 W of cw power in linearly polarized single mode beam. In quasi cw Q-switched regime of operation the average power of the laser was near 2 W with pulse repetition rate of 5 kHz and pulse duration of 400 ns which corresponds to the maximum pulse peak power of about 1 kW. The output beam of the laser was focused by the lens

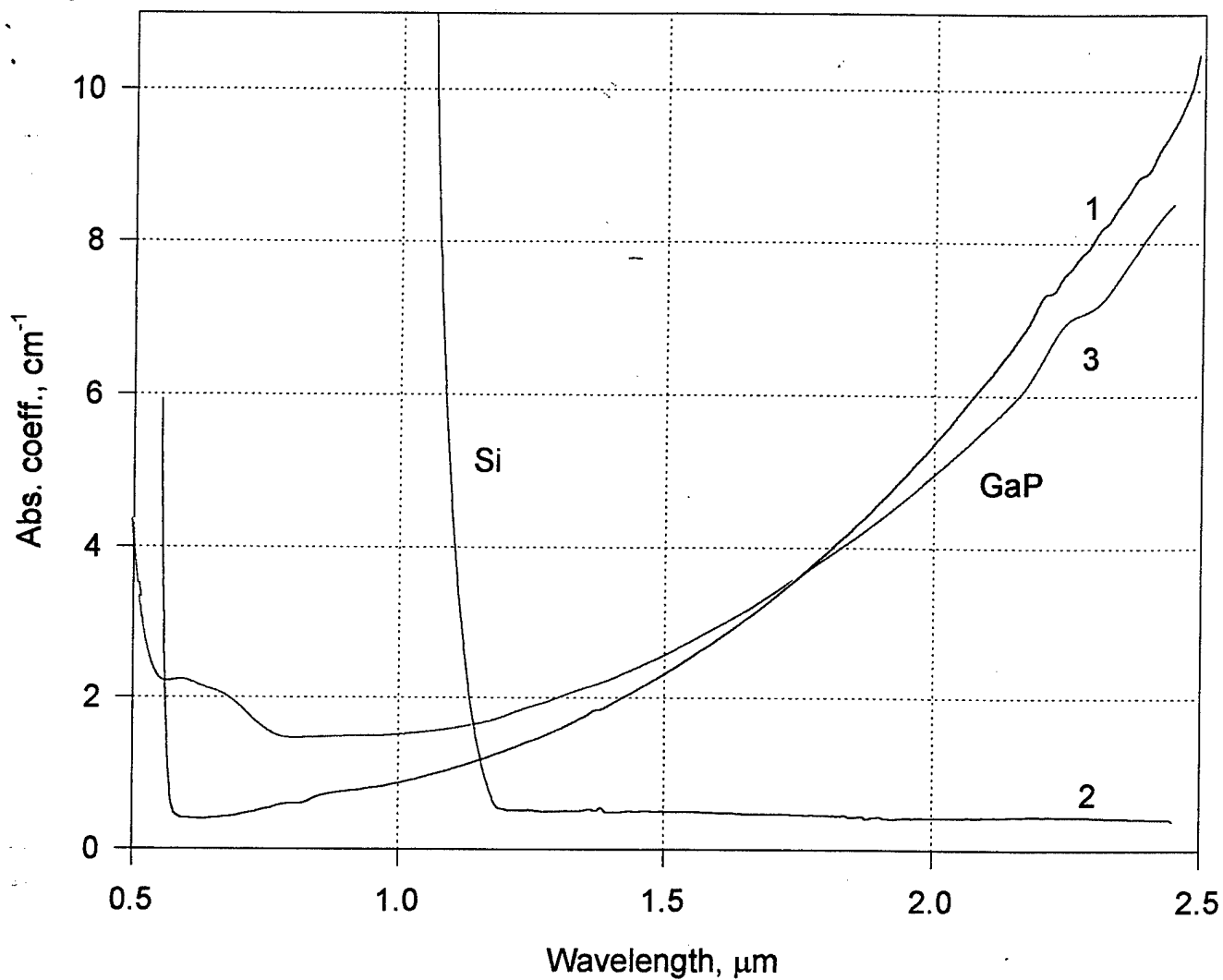


Fig.16 The absorption coefficient of GaP (1,3) and Si (2) samples
 curve 1 - absorption of GaP plate 5 mm thick (Sample 1) with 0.4 mm thick plate (Sample 2) in the compensating channel.
 curve 2 - absorption for Si plate 5 mm thick (Sample 3) with 0.5 mm thick plate (Sample 4) in the compensating channel;
 curve 3 - absorption for GaP plate 4.4 mm thick (Sample 5) with smaller concentration of impurities with 0.75 mm thick plane (Sample 6) in the compensating channel.

with 200 mm focal length to form the prolonged waist with beam diameter of 0.25 mm. The set of calibrated neutral filters was used to modify the incident power keeping the beam shape inside the tested sample unchanged. The thin plates of Si and GaP were placed in the beam's waste and oriented at Brewster angle towards the incident beam to minimize the reflective losses from the sample's edges.

The dependence of transmitted peak power versus the incident peak power for Si plate (Sample 4) is shown in Fig.17 by curve 1 (black circles). For all graphs the upper 'X' axis is recalculated into the pump power density. The curve demonstrates the linear growth of transmitted peak power at low incident peak powers (<0.3 kW) with slope of about 0.5 ($T=50\%$) and is saturated at incident peak powers exceeding 0.4 kW. The growth of sample's absorption at the excitation wavelength should be due to saturation of admixture absorption followed by generation of free carriers in the conduction band. The presence of free carriers results in additional absorption which grows with power density increase. Such behavior is characteristic for materials used for optical limiters.

On the contrary, the shape of the GaP dependence shown in Fig.17 (curves 2, red circles, and curve 3, blue square) remains that for saturable absorbers, as it has two distinguishable linear parts with different slope. The slope of the curve at high incident peak powers characterizes the maximum attainable optical transmission of the sample limited by residual absorption (75%). The curve for the thin plate (Sample 2) demonstrates the slope of ~ 0.47 ($T=47\%$) at low peak powers and of ~ 0.75 ($T=75\%$) at high peak powers. The plate with less concentration of impurity (Sample 6) which was demonstrated by absorption measurements has the slope at initial part of ~ 0.6 ($T=60\%$) and the saturation of absorption starts at a little bit higher peak power compared to the sample with higher concentration of impurities and the maximum optical transmission practically the same as for Sample 2 ($T=75\%$).

The transmission of 5 mm thick cubic sample N1 under the same pump conditions is presented in Fig. 18. Unlike thin plates the thick one demonstrates no nonlinearity in absorption. This can be due to internal block structure of the sample with numerous blocks oriented irregularly each with its own absorption and saturation level.

For $1.32\ \mu\text{m}$ operation the flat-flat optical scheme of Nd:YAG laser was used. As the cross section of the $1.32\ \mu\text{m}$ transition is much less than at the main $1.06\ \mu\text{m}$ transition the output mirror with 97% reflectivity was used. The reflectivity of both total reflecting and output mirrors at fundamental oscillation wavelength ($1.064\ \mu\text{m}$) were less than 20%. The laser emitted ~ 500 mW in pure cw mode and ~ 260 mW in quasi cw mode with pulse repetition rate of 5 kHz and

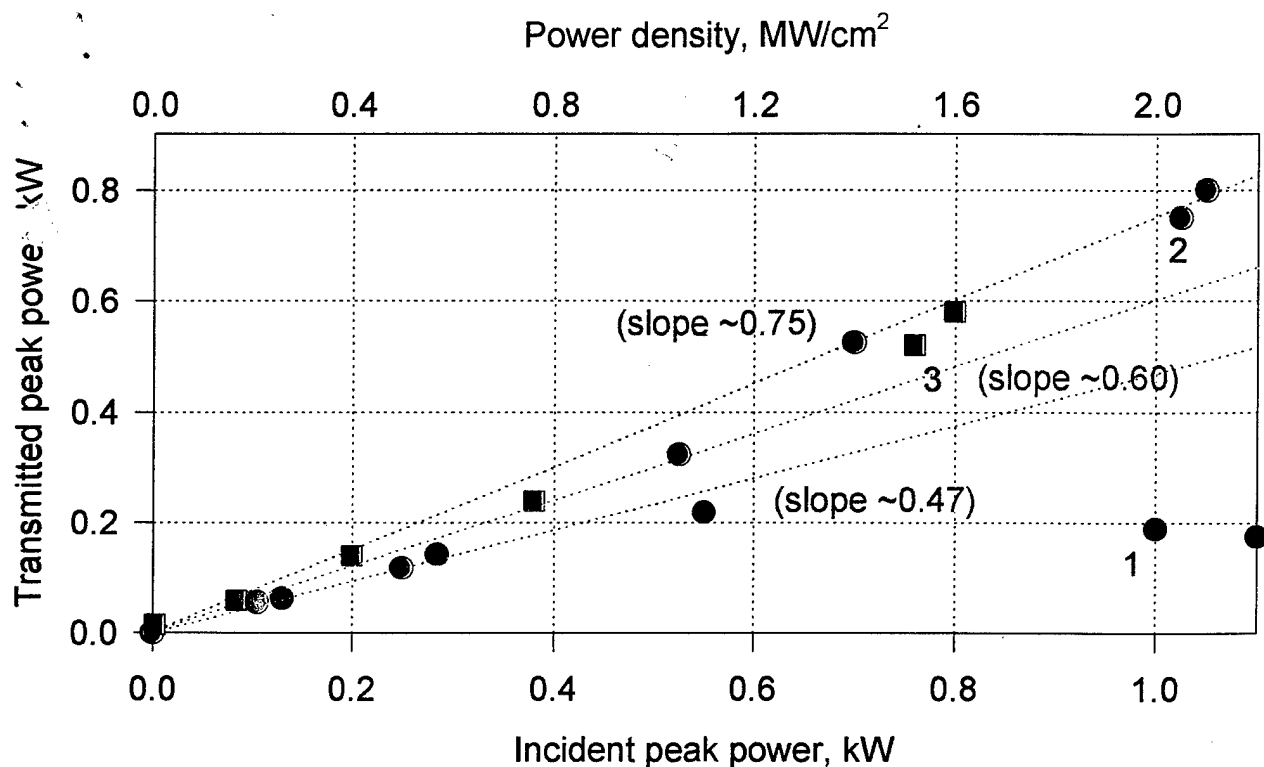


Fig.17 Transmission of Si (1) and GaP(2,3) samples under 1.06 μm excitation of Nd:YAG quasi-cw laser.

curve 2 - GaP plate 0.4 mm thick (Sample 2) with relativeley high impurity concentration,
 curve 3 - GaP plate 0.75 mm thick (Sample 6) with relatively low impurities concentration.

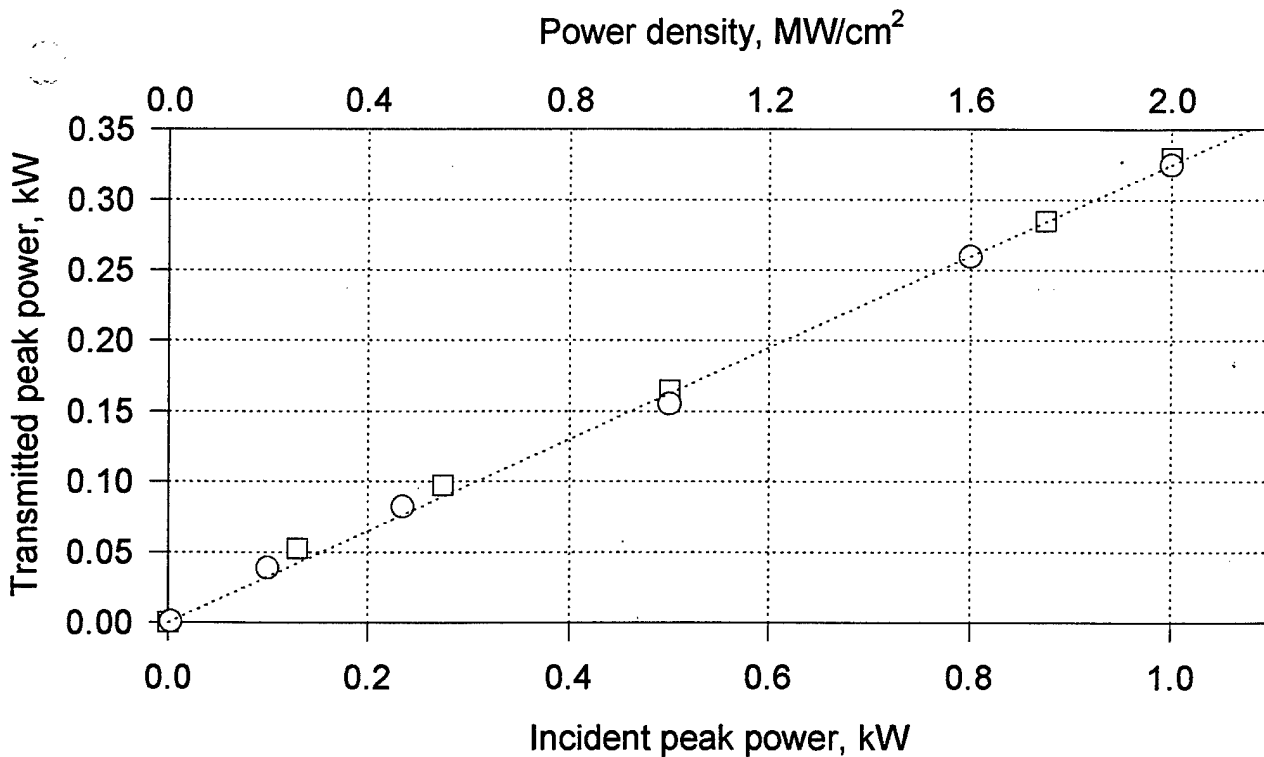


Fig.18 Transmission of 5 mm thick GaP plate (Sample 1) under 1.06 μm excitation of Nd:YAG quasi-cw laser.

pulse duration of 400 ns which corresponds to ~ 130 W of peak power. To increase the power density in the sample the shorter focal length lens (~ 100 mm) was used to focus the pump.

Under the $1.32\ \mu\text{m}$ pump the behavior of the curve shown by curve 1 in Fig. 19 for Si plate (Sample 4) remains that for $1.06\ \mu\text{m}$ pump with transmission decrease at high peak pump powers. The slope of the curve at the initial part is ~ 0.65 ($T=65\%$) which is close to that for $1.06\ \mu\text{m}$ pump - 0.5 ($T=50\%$). For GaP 5 mm thick cubic (Sample 1) the transmission linearly follows the increase of pump peak power and has no noticeable nonlinearity. The slope of the curve is 0.25 ($T=25\%$) which is also close for that for $1.06\ \mu\text{m}$ pump - 0.33 ($T=33\%$).

Infrared laser frequency shifting on KGW Raman crystal

In this set of experiments the KGW Raman crystal $4\times 4\times 40$ mm size was pumped by first ($1.064\ \mu\text{m}$) or second ($0.532\ \mu\text{m}$) harmonic radiation of mode-locked Nd:YAG laser. The scheme of the experimental setup is shown in Fig.20. The Nd:YAG picosecond laser was formed by a master oscillator (1-6) with acousto optical (3) and passive (dye-based) (7) modulators and two stage single pass amplifier (8). The laser emitted the train of approximately 5 pulses with 30 picosecond duration each. The laser radiation was then passed through an adjustable telescope (10) to decrease the spot size and increase pump density and then sent to the Raman crystal (11). The scattered light was collimated by lens, passed through the Lot Oriel monochromator (12) and measured by germanium Ge (for IR pump) or silicon Si (for green pump) photodiode (13).

For the second harmonic $0.53\ \mu\text{m}$ green pumping, three Stokes components were observed $\lambda=560, 590$ and 620 nm. For 1.06 infrared pumping we found that the forward scattered radiation contained at least three Stokes components ($\lambda_{1st}=1.18\ \mu\text{m}$, $\lambda_{2st}=1.32\ \mu\text{m}$, $\lambda_{3st}=1.5\ \mu\text{m}$) and one anti-Stokes component ($\lambda_{1ast}=0.97\ \mu\text{m}$). The dependencies of output energy for three Stokes components on the pump intensity are presented in Fig.21(a) and 22(a) for green and IR pump correspondingly. The solid curves in the Figs. are experimental data approximation used to determine the SRS threshold. The overall output Stokes efficiency is shown in Figs. 21(b) and 22(b) also for green and IR pump. The level of 1% is marked to pick out the threshold pump intensity. The obtained threshold intensities and calculated on their basis threshold gain G_{tr}^{th} are collected in Table 1. The value of the transient threshold gain G_{tr}^{th} averaged using three different pump cases is calculated to be 67 ± 3 being approximately the factor of 2.7 larger than the steady-state threshold gain ($G_{ss}^{th}=25$), which is defined as the point where 1% of the pump intensity has been converted to the Stokes intensity [11]. It should be noted that the corresponding value of transient SRS threshold gain for $\text{Ba}(\text{NO}_3)_2$ crystal under similar condition

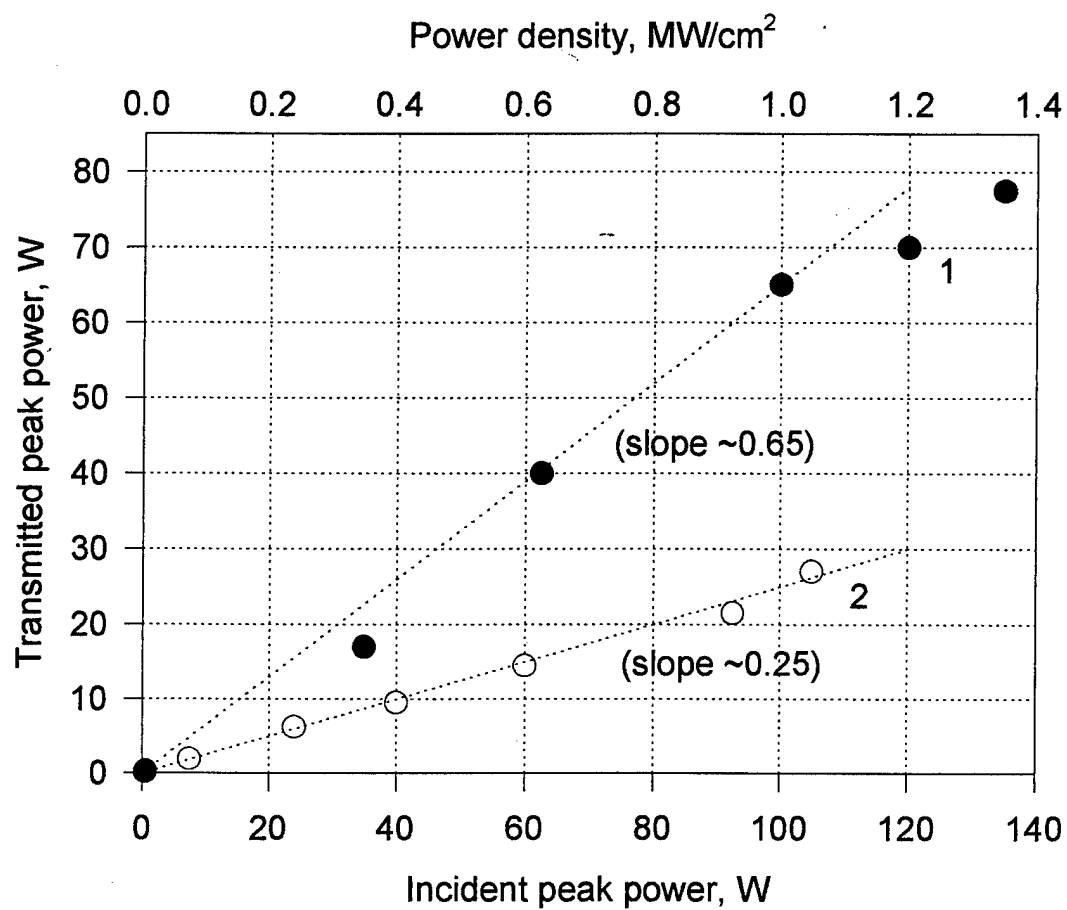


Fig.19 The transmission of Si (1) plate 0.5 mm thick (Sample 4) and GaP (2) plate 5 mm thick (Sample 1) under 1.32 μm pump of quazi-cw Nd:YAG laser.

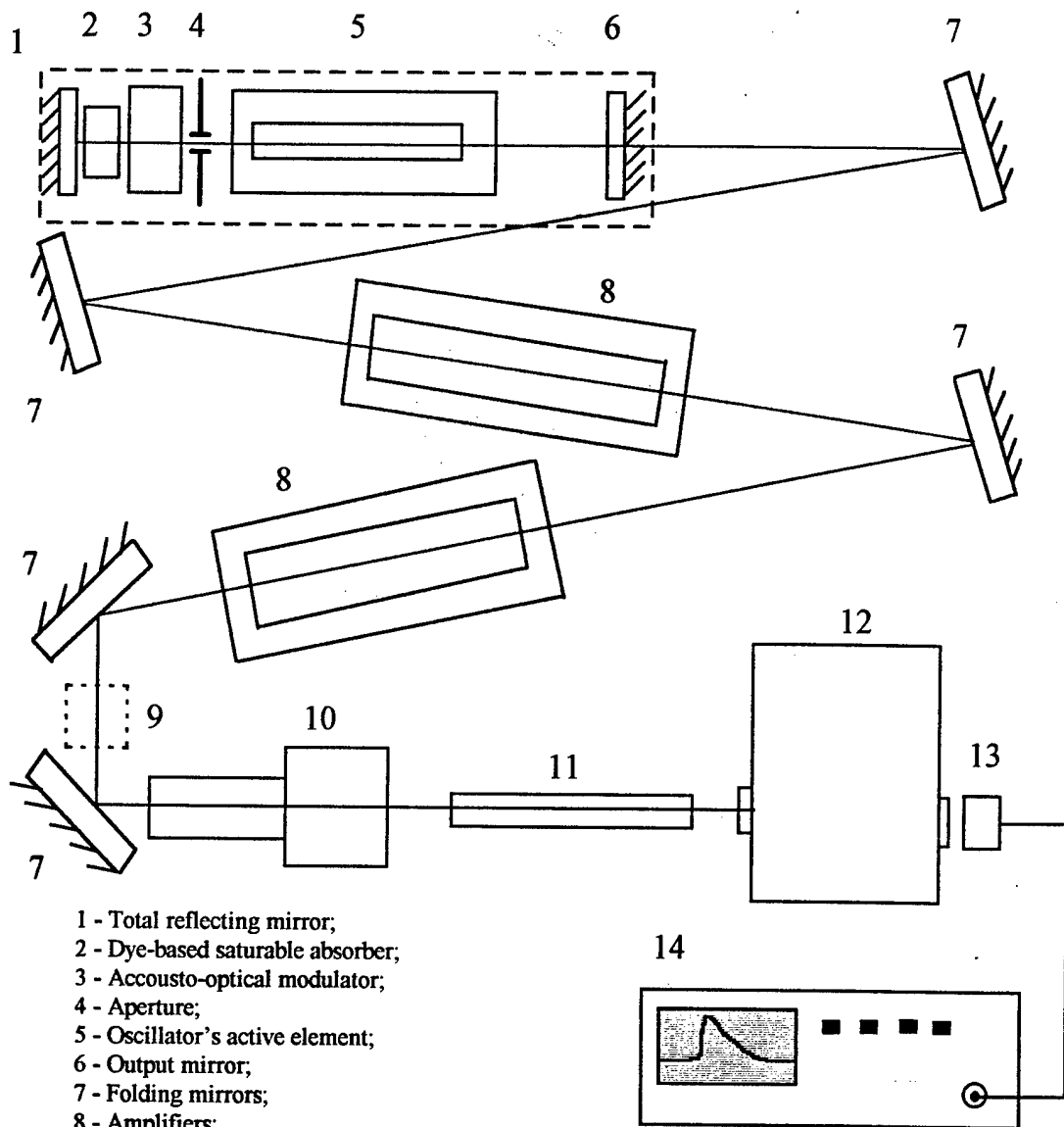


Fig.20

was measured to be $G_r^{th}=260\pm30$ [11] which is about 3 times higher than that for KGW crystal. The observed four times increase of the threshold pump intensity for IR (1.064 μm) radiation compared for that for green (0.53 μm) radiation proves the four fold decrease of Raman gain with two fold increase of pumping wavelength for KGW, which is similar to that for $\text{Ba}(\text{NO}_3)_2$.

We can conclude that efficient SRS both under green and IR laser pump can be obtained for KGW Raman crystal with picosecond pump pulses. The shorter vibrational dephasing time for KGW crystal and higher integral cross-section results in lower thresholds compared to $\text{Ba}(\text{NO}_3)_2$ crystal which is opposite to the case of nanosecond pulse pump. These results show the possibility to use the KGW crystal for Raman shifting of picosecond pulses subsequently from 1.064 μm to 1.18 μm , 1.34 μm and 1.5 μm region with efficiency of 10-20% using the Stokes generation.

Table 6. Measured threshold pump intensities I_p and calculated on their basis threshold SRS gain G_{th} for KGW Raman crystal under IR and green pump.

Pump wavelength λ_p , mm	First Stokes wavelength λ_1 , μm	Pump beam diameter d, mm	Threshold pump intensity I_p , GW/cm^2	Threshold SRS gain G_{th}
0.532	0.560	0.15	0.71	68.2
1.064	1.18	0.15	2.7	64.8
1.064	1.18	0.11	2.9	69.6

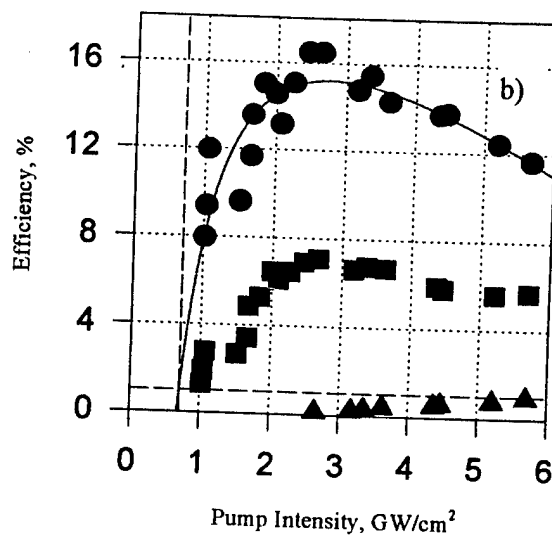
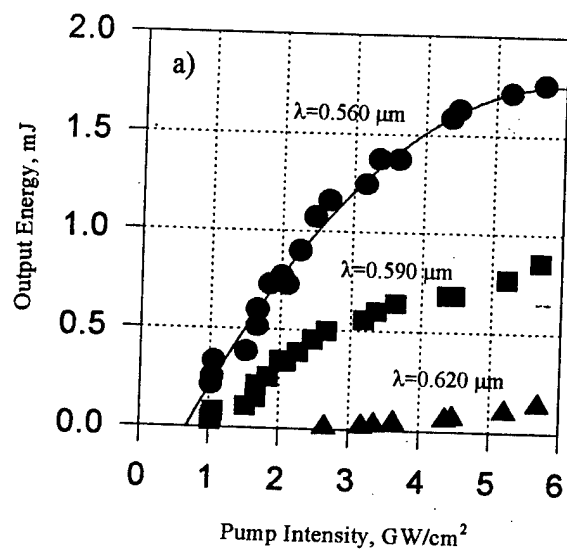
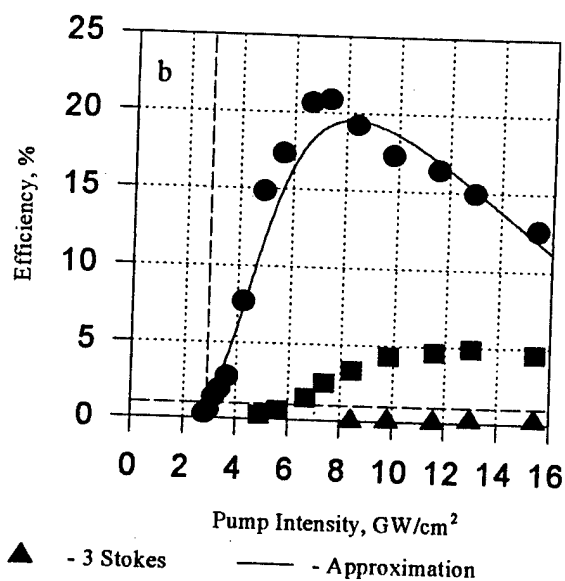
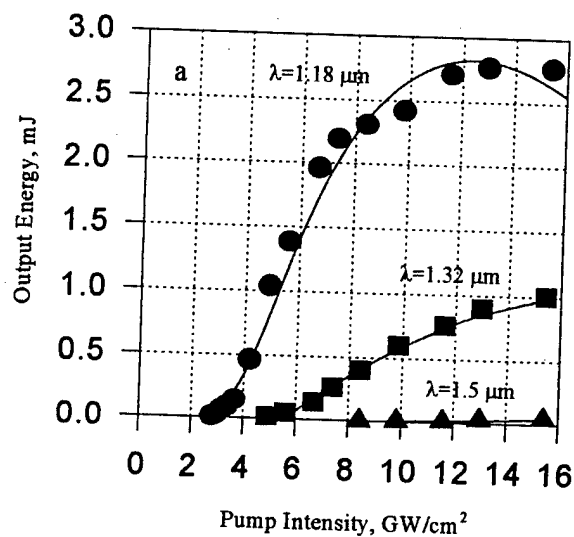


Fig. 21.



● - 1 Stokes ■ - 2 Stokes ▲ - 3 Stokes — - Approximation

Fig. 22

References

1. G. Eckhardt, D. P. Bortfeld, and M. Geller, "Stimulated emission of Stokes and anti-Stokes Raman lines from diamond, calcite and α -sulfur single crystals," *Appl. Phys. Lett.*, **3**, 137 (1963).
2. G. Bisson, G. Mayer. "Effects Raman stimulate's dans la calcite." *Cr.Acad.Sci.(Paris)*, **265**, 397 (1967).
3. K. Park. *Phys. Lett.* **22**, 39 (1966); *Phys. Lett. A25*, 490 (1967).
4. S. N. Karpukhin, A. I. Stepanov. "SRS oscillation in the cavity in $\text{Ba}(\text{NO}_3)_2$, NaNO_3 and CaCO_3 crystals. *Kvantovaya elektronika*, **13**, 1572 (1986), *Sov J. Quantum Electron.* **13**, ??, (1986).
5. G. Eckhardt, *IEEE J. Quantum Electr.*, **QE-2**, 1 (1966).
6. A. S. Eremenko, S. N. Karpukhin, and A. I. Stepanov, "SRS of the second harmonic of neodymium laser in nitrate crystals." *Sov. J. Quantum Electron.*, **10**, 113 (1980).
7. T. T. Basiev, V. N. Voitsekhovskii, P. G. Zverev, F. V. Karpushko, A. V. Lubimov, S. B. Mirov, V. P. Morozov, I. V. Mochalov, A. A. Pavlyuk, G. V. Sinitsyn, and V. E. Yakobson, "Conversion of tunable radiation from a laser utilising an LiF crystal containing F_2^- colour centres by stimulated Raman scattering in $\text{Ba}(\text{NO}_3)_2$ and $\text{KGd}(\text{WO}_4)_2$ crystals," *Sov. J. Quantum Electron.*, **17**, 1560 (1987).
8. P. G. Zverev and T. T. Basiev, "Compact SRS laser on barium nitrate crystal", *Proceedings of All-Union Conference „Laser Optics“*, Leningrad, **2**, 363 (1993).
9. P. G. Zverev, T. T. Basiev, I. V. Ermakov, A. M. Prokhorov, "Stimulated Raman scattering in barium nitrate crystal in the external optical cavity", in *Laser Methods of Surface Treatment and Modification*, SPIE - The International Society for Optical Engineering, **2498**, 164 (1994).
10. J. T. Murray, R. C. Powell, N. Peyghambarian, D. Smith, W. Austin and R. A. Stolzenberger, "Generation of $1.5\mu\text{m}$ radiation through intracavity solid-state Raman shifting in $\text{Ba}(\text{NO}_3)_2$ nonlinear crystals", *Opt. Lett.* **20**, 1017 (1995).
11. P. G. Zverev, J. T. Murray, R. C. Powell, R.J.Reeves, T.T.Basiev. "Stimulated Raman scattering of picosecond pulses in barium nitrate crystals." *Optics Commun.*, **97**, 59 (1993).
12. A. M. Ivanuk, V. A. Sandulenko, M. A. Ter-Pogosyan, P. A. Shakhverdov, V. G. Chervinskii, A. V. Lukin, V. L. Ermolaev. "Intraresonator stimulated Raman scattering in a nanosecond neodymium laser based on potassium gadolinium tungstate." *Optika i Spectroscopiya*, **62**, 569 (1987).

13. A. M. Ivanuk, M. A. Ter-Pogosyan, P. A. Shaverdov, V. D. Belyaev, V. L. Ermolayev, H. P. Tikhonova. "Picosecond light pulses under intracavity stimulated Raman scattering in the active element of neodymium laser." *Optika i Spectroskopiya*, **59**, 950 (1985) (in Russian).
14. Y.R. Shen, *The Principles of Nonlinear Optics*. New York; Wiley, 1984, ch.10.
15. R. L. Carman, F. Shimizu, C. S. Wang, and N. Bloembergen, "Theory of Stokes pulse shapes in transient stimulated Raman scattering," *Phys. Rev.*, **A2**, 60 (1972).
16. Y. Wang, "Theory of stimulated Raman scattering," *Phys. Rev.*, **182**, 482 (1969).
17. M. G. Raymer and J. A. Walmsley, "The quantum coherence properties of stimulated Raman scattering", in *Progress in Optics XXIII*, E. Wolf eds. Amsterdam, Elsevier Science, 259 (1990).
18. Kaiser, Maier, SRS, *Laser Handbook*
19. P. G. Zverev, W. Jia, H. Liu, and T. T. Basiev, *Opt. Lett.* **20**, 2378 (1995).
20. J. Viščakas, I. Močalovas, A. Michailovas, R. Klevcova, A. Riubimovas. *Lietavos Fizikosrinkinys*, 28, 224, 1998.
21. S.A. Solin, A.K. Ramdos. *Phys. Rev.* 1970, B1, p.1687
22. D.W. Posener «The shape of spectral lines: Tables of the Voigt profile.» *Jour. Australian Phys.* 1959, 186-196.